Inorganic Chemistry

pubs.acs.org/IC

Forum Article

Experimental and Computational Insight into the Mechanism of NO Binding to Ferric Microperoxidase. The Likely Role of Tautomerization to Account for the pH Dependence

Maria Oszajca,* Gabriela Drabik, Mariusz Radoń,* Alicja Franke, Rudi van Eldik, and Grażyna Stochel*

Cite This: *Inorg. Chem.* 2021, 60, 15948−15967

Read Online

ACCESS | Metrics & More | Article Recommendations | Supporting Information

ABSTRACT: According to the current paradigm, the metal−hydroxo bond in a six-coordinate porphyrin complex is believed to be significantly less reactive in ligand substitution than the analogous metal−aqua bond, due to a much higher strength of the former bond. Here, we report kinetic studies for nitric oxide (NO) binding to a heme-protein model, acetylated microperoxidase-11 (AcMP-11), that challenge this paradigm. In the studied pH range 7.4−12.6, ferric AcMP-11 exists in three acid−base forms, assigned in the literature as [(AcMP-11)$Fe^{III}(H_2O)$(HisH)] (**1**), [(AcMP-11)Fe^{III}(OH)(HisH)] (**2**), and [(AcMP-11)Fe^{III}(OH)(His^-)] (**3**). From the pH dependence of the second-order rate constant for NO binding (k_{on}), we determined individual rate constants characterizing forms **1**−**3**, revealing only a ca. 10-fold decrease in the NO binding rate on going from **1** ($k_{on}^{(1)}$ = 3.8 × 10^6 M^{-1} s^{-1}) to **2** ($k_{on}^{(2)}$ = 4.0 × 10^5 M^{-1} s^{-1}) and the inertness of **3**. These findings lead to the abandonment of the dissociatively activated mechanism, in which the reaction rate can be directly correlated with the Fe−OH bond energy, as the mechanistic explanation for the process with regard to **2**. The reactivity of **2** is accounted for through the existence of a tautomeric equilibrium between the major [(AcMP-11)Fe^{III}(OH)(HisH)] (**2a**) and minor [(AcMP-11)$Fe^{III}(H_2O)(His^-)$] (**2b**) species, of which the second one is assigned as the NO binding target due to its labile Fe−OH_2 bond. The proposed mechanism is further substantiated by quantum-chemical calculations, which confirmed both the significant labilization of the Fe−OH_2 bond in the [(AcMP-11)$Fe^{III}(H_2O)(His^-)$] tautomer and the feasibility of the tautomer formation, especially after introducing empirical corrections to the computed relative acidities of the H_2O and HisH ligands based on the experimental pK_a values. It is shown that the "effective lability" of the axial ligand (OH^-/H_2O) in **2** may be comparable to the lability of the H_2O ligand in **1**.

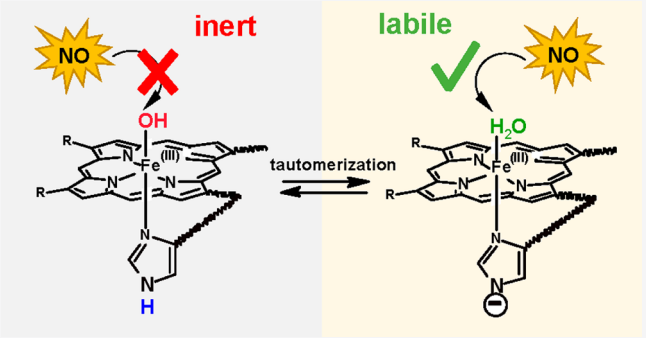

INTRODUCTION

Nitric oxide (NO), due to its involvement in numerous physiological and environmental processes, has been of interest to scientists from various fields of life sciences over the past decades.[1−3] One of the crucial signal transduction pathways of NO occurs via binding to the iron center in heme proteins, making it unsurprising that much attention in the literature was devoted to interactions of this type.[4−6] Studies on the reactivity of NO toward numerous artificial Fe^{III}/Fe^{II} porphyrins provided key information on the mechanisms and factors that govern the reactivity of heme centers,[7−9] whereas quantum-chemical calculations on model systems brought insight into the electronic structure of the resulting metal-nitrosyl complexes.[10,11] In this context, our experimental groups at the Jagiellonian University in Krakow and the University of Erlangen−Nuremberg, involved in a long-term collaboration, contributed a number of studies on NO reactivity with model iron porphyrins and heme proteins, which aimed to unravel the mechanisms of NO activation by its coordination to a metal center.[12−19]

The general mechanistic picture which emerged from the numerous kinetic and spectroscopic studies on iron porphyrin complexes in aqueous solution indicated that despite its radical nature, nitric oxide behaves as a typical nucleophile in ligand-substitution reactions, and thus its reversible binding to the metal center is mainly controlled by the lability of the replaced ligand.[12,20−23] However, in much more catalytically complex biological or environmental systems, numerous other factors such as steric hindrance around the metal center, the type of reaction medium, the chemical nature of the substituted ligand,

Special Issue: Renaissance in NO Chemistry

Received: March 26, 2021
Published: September 3, 2021

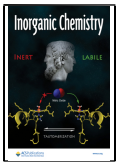

https://doi.org/10.1021/acs.inorgchem.1c00933
Inorg. Chem. 2021, 60, 15948−15967

the electronic and structural properties of other coligands play an important role in controlling the dynamics of the reversible binding of NO.[24]

The overwhelming majority of research, conducted by both us and others, aiming to mimic the interaction of NO with heme proteins, was conducted using artificial porphyrins. Such an approach, through a comparison of the results with the ones obtained for proteins, allows conclusions to be drawn about the degree to which the process is controlled by the metal center, as well as determination of the influence of the protein architecture on the properties of the prosthetic group. Artificial ferric porphyrin (Por) models, which under aqueous conditions exist as diaqua complexes, (Por)Fe(H_2O)$_2$, are very valuable due to the possibility of introducing a variety of modifications to the porphyrin ring periphery. However, they do not fully reproduce the iron coordination center in heme proteins that possesses an amino acid ligand in the fifth-coordination site. Numerous attempts have been made to obtain monoamino acid or amino acid mimics (e.g., imidazole), substituted forms of Fe(III) porphyrins, with varying success,[15,25−27] due to issues of complex stability or thermodynamics of strong field ligand binding (such as imidazole), which result in coordination to both axial sites leading to monosubstituted species to be seldom observed.

Alternatively to synthetic porphyrins, valuable models of the heme protein active center can be obtained by proteolytic digestion of proteins. One of these groups is the family of microperoxidases (MPs), heme-containing peptides with different lengths of the polypeptide chain, obtained from cytochrome *c*. Microperoxidases consist of a ferric protoporphyrin IX covalently attached to a peptide chain, and the fifth coordination position of the iron center is occupied by an imidazole group of histidine. The most commonly used microperoxidases are MP-11 and MP-8, possessing 11- and 8-amino acid peptide chains, respectively. In neutral pH, the sixth-coordination position is occupied by a labile water molecule, which can be easily substituted by various substrates. Microperoxidases are heme enzyme models, which are devoid of distal stabilization mechanisms and kinetic barriers characterizing the structure of the protein. This feature allows assessment of the impact of amino acid residues located on the proximal side of the heme ring on the studied reaction mechanism. MP-11 has been employed in numerous studies devoted to the development of heterogeneous biocatalysts/bioelectrocatalysts and spectroelectrochemical and bioelectronic sensors and devices.[28−33] Furthermore, MPs were the subject of intensive studies on their pH-dependent behavior in aqueous solution,[34−36] reactivity in catalytic oxidation of various substrates,[37−40] and substitution reactions with various ligands.[41−44] However, there are only a few reports available in the literature regarding the pH-dependent reactivity of MPs under alkaline conditions, where successive ionizations of H_2O and HisH ligands result in the accumulation of [Fe^{III}(OH)(HisH)] and [Fe^{III}(OH)(His^-)] species, respectively.[45,46]

Systematic pH-dependent kinetic studies on cyanide binding to MP-8 were reported by Marques et al.[45] Their conclusions concerning the MP-8 reactivity under alkaline conditions were used to assign the [(MP-8)Fe^{III}(OH)(HisH)] species as inert and the [(MP-8)Fe^{III}(OH)(His^-)] species as labile due to the labilization of the Fe−OH bond by deprotonated histidine in the *trans* position.[45] Recently, Ascenzi et al.,[46] in a study devoted to reductive nitrosylation occurring under basic conditions for nonacetylated MP-11, reported rate constants for reversible NO binding. The authors did not observe any clear trend in both rate constants for NO binding (k_{on}) and release (k_{off}) with increasing pH (7.0−9.2) and concluded that these reactions are essentially pH independent. The lack of a pH dependence of k_{on} is per se interesting in view of the paradigmatic inertness of the [(MP-11)Fe^{III}(OH)(HisH)] form, but this aspect was not discussed in ref 46.

In order to better understand at the molecular level how the proximal site of the heme center influences the reactivity with NO, we decided to undertake detailed kinetic and mechanistic studies on NO binding with the application of acetylated MP-11 (AcMP-11). *N*-acetylation prevents the pronounced aggregation of this heme enzyme model.[47] To answer the question of how the ionization of coordinated water and histidine affects the properties of the heme center toward NO binding, the kinetic studies were performed over a wide pH range, 7.4−12.6 (Figure 1), which was crucial to obtaining more mechanistic details governing the reactivity of various MP-11 forms.

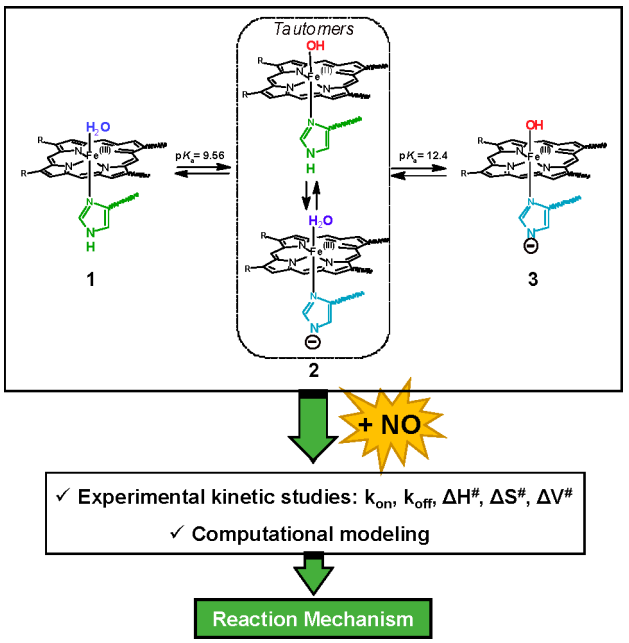

Figure 1. General concept of this study. Values of pK_a for AcMP-11 were taken from the work by Marques et al.[35]

As will be discussed in detail below, the determined pH-dependent kinetic profile reveals a surprisingly high reactivity of the [(AcMP-11)Fe^{III}(OH)(HisH)] form and inertness of the [(AcMP-11)Fe^{III}(OH)(His^-)] form, previously thought to be much more reactive than the [(AcMP-11)Fe^{III}(OH)(HisH)] one. According to the current paradigm, six-coordinate porphyrin complexes of the [(AcMP-11)Fe^{III}(OH)(HisH)] form are expected to be inert, and their reactivity should be limited by the dissociation of the OH^- ligand. This picture is challenged by the presently observed second-order rate constant for the alkaline species [(AcMP-11)Fe^{III}(OH)(HisH)], which is only 10 times smaller than the one measured for the labile [(AcMP-11)Fe^{III}(H_2O)(HisH)] form. In order to interpret this intriguing behavior, experimental studies were supported by quantum-chemical calculations. The obtained results lead to the proposition of a new mechanism that governs the reactivity of six-coordinate heme centers

https://doi.org/10.1021/acs.inorgchem.1c00933
Inorg. Chem. 2021, 60, 15948−15967

containing two protic ligands: H_2O/OH^- and HisH/His^-. In this mechanism, the $[(AcMP\text{-}11)Fe^{III}(OH)(HisH)]$ species remains in equilibrium with its less stable but kinetically labile tautomer $[(AcMP\text{-}11)Fe^{III}(H_2O)(His^-)]$, which is responsible for the facile ligand-exchange reactivity. The feasibility of the presence of the $[(AcMP\text{-}11)Fe^{III}(H_2O)(His^-)]$ tautomer fraction is supported by theoretical calculations. The contribution of the tautomer fraction provides a logical explanation for the experimentally observed pH-dependent reactivity profile of AcMP-11. In the context of quantum-chemical calculations, which will be reported here, we notice that, despite the abundance of theoretical studies for porphyrins and models of enzymatic active sites, there have been so far only a few quantum-chemical studies directly referring to the properties of MPs.[48−51] Moreover, there exist substantial challenges with reliable computational description of the spin-state energetics for the ferric site in MP, the relative acidities of the axial ligands bound to it, and the solvation effects on the electronic structure and ligand binding properties. These issues will be, therefore, addressed below, including detailed comparison of the computed properties with the experimental data.

EXPERIMENTAL AND COMPUTATIONAL DETAILS

Materials. All chemicals used in this study were of analytical reagent grade. Microperoxidase-11 (>85%; MP11), 3-(cyclohexylamino)-1-propanesulfonic acid (CAPS), 2-amino-2-hydroxymethylpropane-1,3-diol (TRIS), potassium phosphate monobasic, and $NaClO_4$ were purchased from Sigma-Aldrich and used as received. $K[Ru(edta)Cl]\cdot 2H_2O$ was synthesized according to the published procedure.[52] NO gas was purchased from Linde Gaz Polska sp. z. o. o., bubbled through a concentrated KOH solution to remove higher nitrogen oxides (N_2O_3, NO_2), and then passed through an Ascarite II column (NaOH on silica gel, Sigma-Aldrich).

Solution Preparation. Microperoxidase-11 (MP-11) was acetylated according to a published procedure in order to prevent aggregation in an aqueous solution.[34] After acetylation, AcMP-11 was purified by dialysis using a Pur-A-Lyser Dialysis Kit, MWCO 1 kDa (Sigma-Aldrich). HPLC analysis of the reaction mixture revealed the conversion of MP-11 to AcMP-11 to be close to 100% (Figure S1, Supporting Information). The HPLC analysis was performed using a PerkinElmer HPLC Chromera system equipped with a diode-array detector. Separation was performed on a Brownlee Bio C18 PerkinElmer (5 μm, 150 mm × 4.6 mm) column. Samples were eluted with a gradient method: CH_3CN SuperGradient + 0.05% TFA/H_2O + 0.05% TFA − 10/90, gradient to 40/60 for 20 min with a flow rate of 1 mL/min. Samples of AcMP-11 were prepared at pH 7.4 using TRIS or phosphate buffers and at pH 10.0−11.5 using CAPS buffer solutions (0.05 M). pH measurements were performed on an Elmetron pH meter (CP-401) calibrated with certified, HANNA standard buffer solutions. In experiments at higher pH (pH > 11.5), an appropriate concentration of NaOH was used. The ionic strength of the buffer solutions was adjusted with $NaClO_4$ to 0.15 M. For temperature dependent kinetic studies, the temperature dependence of the pK_a of the applied buffer was taken into consideration, and the buffer pH was set for each temperature individually. Argon and gastight glassware were used for preparation and handling of deoxygenated solutions. Deionized water was used for the preparation of all solutions. Spectrophotometric analyses were performed on Lambda 950 and Lambda 35 PerkinElmer spectrophotometers.

Laser Flash Photolysis Measurements. The laser flash photolysis technique was applied for the kinetic studies at a pH of 7.4. The experiments were carried out with the use of the LKS.60 Applied Photophysics spectrometer and a Nd:YAG laser (SURLITE I-10 Continuum). Excitation was at 355 nm (the third harmonic of the laser). Absorbance changes were monitored at 415 nm using a xenon arc lamp, a monochromator, and a photomultiplier tube (PMT-1P22). The absorbance reading was balanced to zero before the flash, and data were recorded on a digital storage oscilloscope, DSO HP 54522A, and then transferred to a computer for analysis. Reported rate constants are the average of several kinetic traces. High-pressure laser flash experiments were performed in the pressure range of 5−150 MPa.[19] Gastight quartz cuvettes and a pillbox cell combined with high-pressure equipment[53] were used at ambient and under high pressure, respectively.

Stopped-Flow Measurements. Ambient-pressure stopped-flow measurements were performed on a thermostated (±0.1 °C) Applied Photophysics stopped-flow SX20 instrument. The reaction kinetics were studied under pseudo-first-order conditions applying at least a 10-fold excess of [NO] over AcMP-11. The kinetics of the reaction were monitored at 415 nm. The rates of NO release (k_{off}) were determined by an NO-trapping method. As reductive nitrosylation occurs under basic conditions for the AcMP-11 nitrosyl derivative, reactions of $[(AcMP\text{-}11)Fe^{II}(NO^+)(His)]$ with $[Ru^{III}(edta)]^-$ under basic conditions were performed on the stopped-flow apparatus equipped with a sequential mixing mode (Applied Photophysics SX20). This involved rapid mixing of the AcMP-11 complex with NO solutions in the first mixing drive. After a defined delay period (5 s), the aged solution was mixed with the $[Ru^{III}(edta)]^-$ solution in the second mixing drive, and the reaction was followed spectrophotometrically. The kinetics of NO release was followed at 415 nm. The pH-dependent spectra for the nitrosylated form of microperoxidase were also registered with the application of the stopped-flow apparatus in combination with a diode-array detector. It was used because it is impossible to perform a direct spectrophotometric titration of $[(AcMP\text{-}11)Fe^{II}(NO^+)(His)]$ due to the instability of the nitrosyl complex toward subsequent reductive nitrosylation. Spectra at various pH values were registered by mixing aqueous solutions of nitrosyl species with buffer solutions of a set pH value. Experimental data were fitted to the sigmoidal equation (OriginPro 2019: Category, Growth/Sigmoidal; Function, DoseResp; Iteration Algorithm, Levenberg−Marquardt) to evaluate the pK_a according to the equation:

$$y = A_{min} + \frac{A_{max} - A_{min}}{1 + 10^{(\log x_0 - x)*p}}$$

where y is the absorbance at the selected wavelength registered at a particular pH, A_{min} and A_{max} represent the corresponding minimum and maximum absorbance, $\log x_0 = pK_a$ represents the center of the Hill slope, and p is the Hill coefficient of the slope obtained from the plot measured at the inflection point. High-pressure stopped-flow experiments were performed in the pressure range of 10−130 MPa on a custom-built apparatus.[54,55] OLIS KINFIT software (Bogart, GA, 1989) was used for the analysis of the kinetic traces.

Computational Methods and Models. The ferric site of AcMP-11 was modeled at three levels of structural complexity (Figure 2). In the simplest model, model #1, the heme group was reduced to Fe^{III} porphin (unsubstituted ring) with appropriate axial ligands: imidazole (ImH/Im^-) and H_2O (species **1**, **2b**)/OH^- (**2a**, **3**)/NO (**X**, **Y**)/nothing (**A**, **B**). The molecular species **1**, **2a**, **2b**, **3**, **X**, and **Y** are defined in Scheme 1, whereas **A** and **B** are five-coordinate species with either HisH or His^- ligand. Model #2 adds explicit water (solvent) molecules hydrogen-bonded to the axial ligands: one to ImH/Im^- and two to H_2O/OH^-. Depending on the protonation state of the axial ligand, the added waters are either donors or acceptors of the hydrogen bond. For the computation of the H_2O dissociation energy, the released H_2O molecule was explicitly solvated in the same way (Figure S2, Supporting Information) to preserve the pattern of hydrogen bonding. The most extensive model, model #3, was obtained by extending model #2 with a part of the peptide backbone (Cys14-Ala15-Gln16-Cys17-His18) and side substituents of the heme. Starting coordinates for geometry optimization were obtained from the crystal structure of the parent cytochrome *c* (PDB code: 3NBS). By experimentation, we found that explicit solvation must be introduced also for heme propionates (four waters) and the carbonyl group of Cys17 (one water, interacting also with the water bound to

https://doi.org/10.1021/acs.inorgchem.1c00933
Inorg. Chem. 2021, 60, 15948−15967

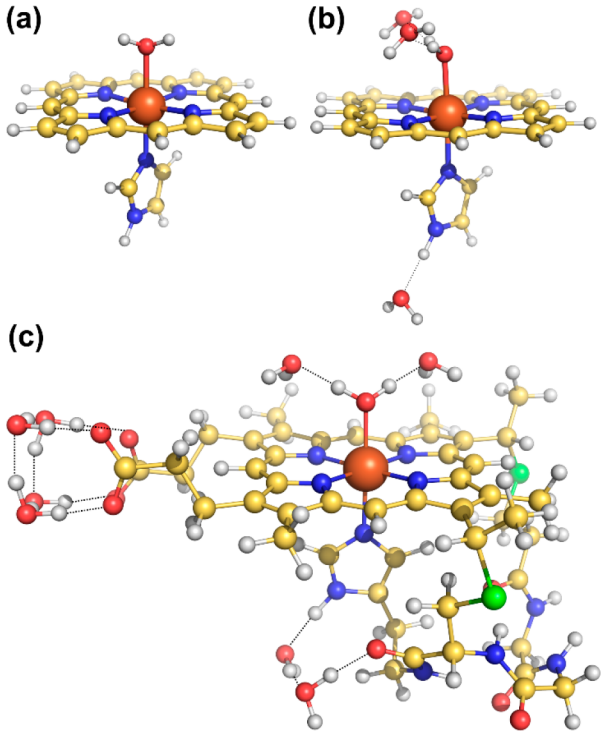

Figure 2. Molecular models #1 (a), #2 (b), and #3 (c) for the example of complex **1**, i.e., [$Fe^{III}(H_2O)$(HisH)], in the sextet state. Colors of atoms: Fe, orange; C, yellow; O, red; N, blue; H, white; S, green.

the His-18 ligand) in order to avoid artifacts during the geometry optimization. The same peptide conformation and hydrogen-bonding pattern were preserved in all modeled structures and spin states. All optimized structures can be found in the Supporting Information.

As shown in the literature, side substituents of the ring[56] and hydrogen bonding with the axial ligands[57−59] can considerably influence the electronic properties of iron porphyrins. Indeed, we observed (Table S1, Supporting Information) that the explicit solvation introduced in model #2 strongly influences water dissociation energies from complexes **1** and **2b** (by 30 kJ/mol) and the tautomerization energy of **2a** into **2b** (by 10 kJ/mol), which are the key energetic properties for the mechanistic considerations given below. The hydrogen bonding also influences relative spin-state energetics of iron (Table S1), although the effect is smaller than in other cases reported in the literature.[59,60] Switching from model #2 to #3 alters the mentioned properties by only a few kilojoules per mole, suggesting that the results are approaching convergence with respect to the model size.

All calculations at the DFT or DFT-D3 level (D3 with Becke-Johnson damping[61]) were performed using Gaussian 09.[62] Unless stated otherwise, the calculations were performed within the polarizable continuum model of water (IEF-PCM with the UFF atomic radii).[63] The calculations were spin-unrestricted, but without significant spin contamination. Geometries were optimized at the B3LYP-D3/def2-TZVP level for structural models #1 and #2, but at the B3LYP-D3/def2-SV(P) level for the larger model #3 (~150 atoms), in all cases using FineGrid. Subsequent single-point calculations for model #2 were carried out using four DFT methods (B3LYP-D3, B3LYP*-D3, TPSSh-D3, and M06L) with a larger ma-TZVPP basis set and UltraFine grid. The energies obtained in such a way from each DFT method ($E^{\text{method/ma-TZVPP}}_{\text{model\#2}}$) were additively corrected for scalar-relativistic effects (ΔE_{rel}) as well as for "peptide matrix" and substituent effects introduced in model #3 ($\Delta E_{\text{peptide}}$):

$$E^{\text{method}}_{\text{final}} = E^{\text{method/ma-TZVPP}}_{\text{model\#2}} + \Delta E_{\text{rel}} + \Delta E_{\text{peptide}} \quad (1)$$

where the ΔE_{rel} term is the difference between the B3LYP/cc-pVTZ-DK (DKH relativistic) and B3LYP/cc-pVTZ (nonrelativistic) single-point energies for the B3LYP-D3/def2-TZVP geometry of model #2; the $\Delta E_{\text{peptide}}$ term is the difference between the B3LYP-D3/def2-TZVP//B3LYP-D3/def2-SV(P) energies for model #3 and model #2. Additional results corresponding to the SMD solvation model[64] were obtained by correcting energies of eq 1 for a difference between the SMD and PCM single-point B3LYP/def2-TZVP energies for model #2. Total energies can be found in the Supporting Information.

Electronic energies resulting from eq 1 were corrected by adding either vibrational zero-point energy (ZPE) or suitable thermochemical correction (enthalpy H or Gibbs free energy G) based on the B3LYP-D3/def2-TZVP harmonic frequency calculations for model #1, a temperature of 298 K, and a pressure of 1 atm. For ΔG computation, the quasi-harmonic approximation with the 50 cm^{-1} cutoff was used to correct the vibrational partition function for artifacts related to low-frequency modes, whose entropies are ill-described by the harmonic approximation. Moreover, in order to obtain realistic ΔG values for the ligand-removal reactions in water, the translational and rotational entropy contributions to ΔG were scaled down to 50% of their gas-phase values (the Wertz correction).[65−67] This approach automatically accounts for[66] the change of standard state from ideal gas (internally used in Gaussian) to a 1 M solution (used for all ΔG values reported here).

To accurately describe spin-state energetics, we propose here the DFT+ΔCC approach, which is based on our previous computational work with heme-related models using coupled cluster methods.[68,69] The DFT+ΔCC are obtained from DFT energies of eq 1 by adding a correction term to reduce the error in predicted spin-state energetics:

$$E^{\text{method+}\Delta\text{CC}}_{\text{final}} = E^{\text{method}}_{\text{final}} + (E^{\text{UCCSD(T*)-F12a}}_{\text{model\#0}} - E^{\text{method/ma-TZVPP}}_{\text{model\#0}}) \quad (2)$$

The correction term is obtained by comparison of the energy predicted by a given DFT method with the energy from explicitly correlated UCCSD(T*)-F12a[70] method for simplified model #0. Models #0 were obtained from respective models #1 by replacing the ImH/Im^- ligand with NH_3, and resulting geometries were optimized at the B3LYP-D3/def2-TZVP level under the C_s point group (Figure S3, Supporting Information). All calculations for models #0 were performed in a vacuum. The UCCSD(T*)-F12 calculations were performed with Molpro[71] based on the ROHF reference and employing the basis sets defined in Table S2 of the Supporting Information.

For DFT calculation of the reaction energies, we initially assumed the HS state for all ferric species to minimize the DFT-related errors on spin conversions. Such HS channel DFT results (Table S3, Supporting Information) were subsequently corrected for the actual spin-state energetics based on the DFT+ΔCC results. This was done by correcting (separately for each reactant or product, i) the thermochemical functions of the pure HS state (G^{HS}_i, H^{HS}_i) into spin-unresolved functions (G_i, H_i) corresponding to the ensemble of all spin states at T = 298 K:

$$G_i = G^{\text{HS}}_i + RT \ln p^{\text{HS}}_i \quad (3)$$

$$H_i = H^{\text{HS}}_i + (H^{\text{LS}}_i - H^{\text{HS}}_i)p^{\text{LS}}_i + (H^{\text{IS}}_i - H^{\text{HS}}_i)p^{\text{IS}}_i \quad (4)$$

where p^s_i, the equilibrium population of a spin state s for species i,

$$p^s_i = \frac{\exp(-G^s_i/RT)}{\sum_{s'} \exp(-G^{s'}_i/RT)} \quad (5)$$

is based on reliable DFT+ΔCC spin-state energetics. As might be expected, the resulting corrections (Table S4, Supporting Information) are small for ferric species which are predominantly HS under the experimental conditions (**1**, **2b**, **A**, **B**), but become important for **2a** and **3**. In the latter case, the "ensemble corrections" simply serve to correct for the enthalpy/free energy difference between the HS state and the actual (LS) ground state of **3**.

https://doi.org/10.1021/acs.inorgchem.1c00933
Inorg. Chem. 2021, 60, 15948−15967

The pK_a values were computed both directly[72,73] (from the ΔG of deprotonation, assuming the literature value of −1138.8 kJ/mol for the free energy of the solvated proton[72]) and using the proton exchange (PE) method[72] with a suitable reference, namely, H_2O/OH^- (for deprotonation of the aqua ligand) or ImH/Im^- (for deprotonation of the histidine ligand):

$$pK^{PE}_{a,HA/A^-} = pK^{direct}_{a,HA/A^-} + (pK^{exptl}_{a,HRef/Ref^-} - pK^{direct}_{a,HRef/Ref^-}) \quad (6)$$

where HA/A^- is the acid/base pair of interest, $HRef/Ref^-$ is the reference, and superscript "exptl" denotes the experimental value. The references for pK_a computation were explicitly solvated by three (H_2O/OH^-) or two (ImH/Im^-) waters (Figure S4, Supporting Information) to maintain similarity with the environments of these ligands in our models for microperoxidase.

RESULTS AND DISCUSSION

Kinetic Studies as Function of pH. Kinetic studies on the pH dependent reactivity of AcMP-11 toward NO were performed in the pH range from 7.4 to 12.6. Marques et al. reported that, in this pH range, AcMP-11 exists in three acid/base forms (**1**−**3**), related to successive deprotonations of coordinated water and HisH (Scheme 1).[35] Form **1** has been characterized as [(AcMP-11)$Fe^{III}(H_2O)$(HisH)] and the doubly deprotonated form **3** as [(AcMP-11)Fe^{III}(OH)(His^-)] species. The singly deprotonated form **2** has been characterized as [(AcMP-11)Fe^{III}(OH)(HisH)] (**2a**). However, our mechanistic considerations below will reveal the crucial role of the minor species [(AcMP-11)$Fe^{III}(H_2O)(His^-)$] (**2b**), which is in tautomeric equilibrium with the major species **2a**. It is crucial to emphasize that the equilibrium between tautomers **2a** and **2b** coexisting in form **2** of microperoxidase is pH-independent; therefore, the experimental kinetic data as a function of pH can be used only to characterize the reactivity of form **2** (i.e., the mixture of the two tautomers), not individual reactivities of the two tautomers.

Scheme 1. Reactivity Pattern for AcMP-11 with NO; Molecular Identities of Forms 1−3 and p$K_{a1,2}$ Values According to ref 35, p$K_{a(NO)}$ Value Determined in This Work

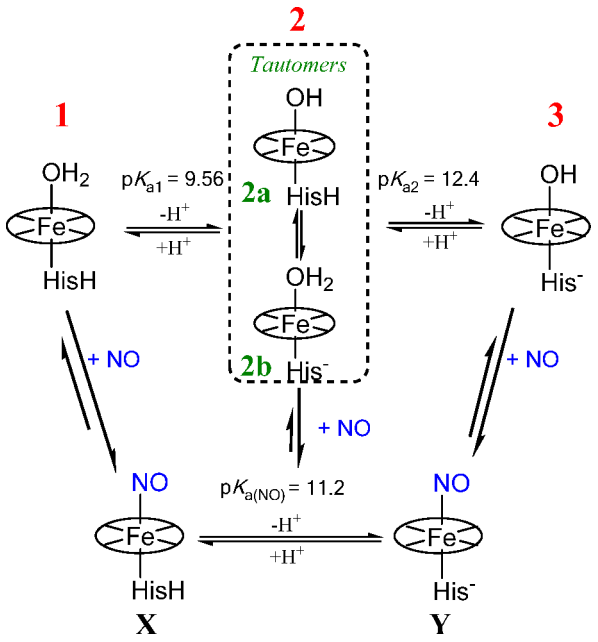

Reversible binding of NO to AcMP-11 at pH 7.4 leads to the formation of a six-coordinate complex, which can be formally represented as [(AcMP-11)$Fe^{II}(NO^+)$(HisH)]. The product has Soret and Q bands at 415, 530, and 560 nm, respectively (Figure S5). When AcMP-11 reacts with NO in the pH range 9−10, where a significant fraction of **2** is present, no changes in the positions of the Soret and Q bands were observed for the nitrosylation product when compared to the product obtained at pH 7.4. This indicates that NO substitutes H_2O/OH^- on coordinating to the iron center, forming [(AcMP-11)-$Fe^{II}(NO^+)$(HisH)] (Scheme 1). A noticeable shift toward longer wavelengths in the Soret band was observed only at pH > 10. The electronic absorption spectra registered at pH > 10 were the same regardless of the procedure applied for the product formation: (i) after the reaction of buffered solutions of AcMP-11 and NO or (ii) in the pH-jump experiment, collected immediately after mixing the unbuffered solution of [(AcMP-11)$Fe^{II}(NO^+)$(HisH)] with the CAPS buffer (e.g., pH 11.0) (Figure S6). The pK_a value of 11.2, estimated from UV−vis spectral changes registered for nitrosylated AcMP-11, was assigned to the deprotonation of HisH (Figure 3, Scheme 1). It is important to note that, under alkaline conditions, the formation of Fe^{II}−NO^+ species is followed by a reductive nitrosylation step, occurring on a much longer time scale and corresponding to the blue-shift of the Soret band maxima (407 nm) as well as absorbance collapse (Figure S7).

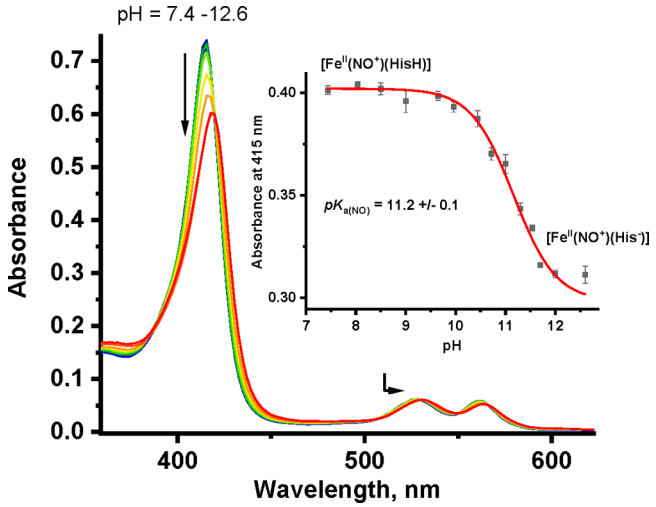

Figure 3. pH dependent UV−vis spectral changes for the nitrosyl complex of AcMP-11 in buffer solutions. Inset: plot of absorbance changes at 415 nm vs pH. Experimental conditions: [AcMP-11] = 5×10^{-6} M (Inset - [AcMP-11] = 2.5×10^{-6} M), [NO] = 2.8×10^{-4} M; buffers used, pH 7.4−9 Tris 0.05 M, pH 9.5−11.5 CAPS 0.05 M, pH 12.0−12.6 NaOH; I = 0.15 M ($NaClO_4$); 20 °C.

At pH 7.4, kinetic studies under pseudo-first-order conditions (applying at least 10 times excess of [NO] over [AcMP-11]) were performed with the stopped-flow technique and laser-flash photolysis (**7**).Kinetic traces recorded with both

$$H_2O + [(AcMP\text{-}11)Fe^{II}(NO^+)(HisH)] \underset{k_{off}}{\overset{h\nu;\ k_{on}}{\rightleftharpoons}} [(AcMP\text{-}11)Fe^{III}(H_2O)(HisH)] + NO \quad (7)$$

techniques exhibited a single exponential behavior and the observed rate constants showed a linear dependence on [NO] ($k_{obs} = k_{on}[NO] + k_{off}$) (Figure 4). The rate constant k_{on} =

https://doi.org/10.1021/acs.inorgchem.1c00933
Inorg. Chem. 2021, 60, 15948−15967

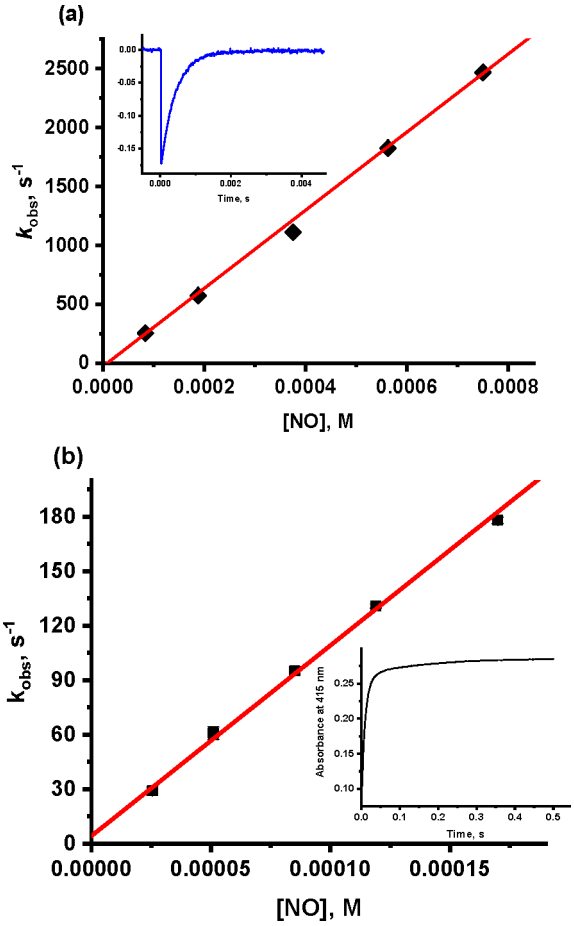

Figure 4. Plots of k_{obs} versus [NO] for the reaction of AcMP-11 with nitric oxide. (a) Dependence obtained with laser flash photolysis technique at pH 7.4, inset: example of registered kinetic trace. Experimental conditions: [AcMP-11] = 5 × 10^{-6} M, I = 0.15 M ($NaClO_4$), pH 7.4 (phosphate buffer 0.05 M), λ_{ex}= 355 nm, λ_{abs}= 415 nm, 20 °C. (b) Dependence obtained with stopped-flow technique at pH 10.4, inset: example of registered double-exponential kinetic trace. Experimental conditions: [AcMP-11] = 2.5 × 10^{-6} M, I = 0.15 M ($NaClO_4$), pH 10.4 (CAPS 0.05 M), 20 °C.

(3.77 ± 0.03) × 10^6 M^{-1} s^{-1} determined from the stopped-flow measurements at 20 °C is in good agreement with the value obtained from flash-photolysis measurements, viz., k_{on} = (3.31 ± 0.04) × 10^6 M^{-1} s^{-1}. The obtained values are higher than the k_{on} = 1.1 × 10^6 M^{-1} s^{-1} value reported by Sharma et al.[74] and k_{on} = 7.8 × 10^5 M^{-1} s^{-1} recently reported by Ascenzi et al.[46] Both authors performed the NO binding studies using nonacetylated MP-11, which most probably is the reason for the discrepancies. Analogous measurements of k_{obs} conducted at higher pH, using only the stopped-flow technique, revealed that, in the pH range of 8.5 to 11.5, kinetic traces exhibited a double exponential character with a very fast NO-concentration-dependent first reaction step and a much slower NO-concentration-independent second reaction step (Figure 4b, inset).

The double exponential character of the kinetic traces was assigned to the presence of a small fraction of aggregates formed under alkaline conditions that participate in reactions with NO alongside the monomer. It is important to stress that under the applied AcMP-11 concentration used for the studies of NO binding, contribution of the second [NO] independent reaction step is very small, thus the fraction of aggregates formed is estimated to constitute only up to a few percent of the AcMP population (for further details, see section Behavior of AcMP-11 in Alkaline Solution). A double-exponential function was applied to fit the kinetic traces in the pH range 8.5−11.5, which allowed determination of the k_{obs} value corresponding to monomer reactivity and the k'_{obs} value corresponding to the reactivity of the aggregates. Measurements of k_{obs} vs [NO] at selected pH values showed a linear dependence and allowed the determination of the second-order rate constant (k_{on}) for the first, fast reaction step, corresponding to the reactivity of monomer AcMP-11, as a function of pH (Figure 5 and Table S5, Supporting Information).

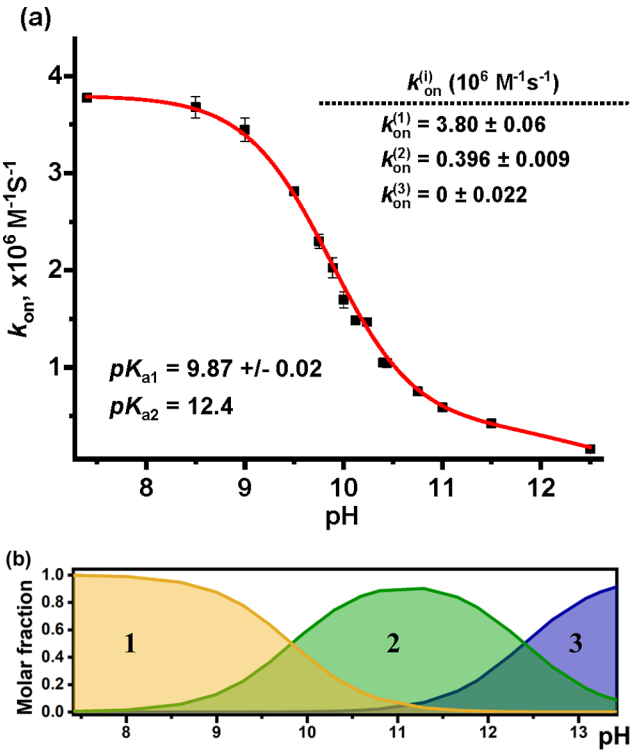

Figure 5. (a) Dependence of k_{on} on pH for the fast reaction step of NO binding to AcMP-11. The line shown was obtained by fitting to the experimental data, the function defined by eqs 8 and 9 with the $k^{(i)}_{on} \geq 0$ constraint, pK_{a1} being a parameter, pK_{a2} being constant 12.4 (ref 35); the resulting $k^{(i)}_{on}$ and pK_{a1} values are annotated. Other attempts to fit this pH dependence (see Figure S9 Supporting Information) lead to similar values for $k^{(i)}_{on}$. (b) Molar fraction of forms **1**, **2**, and **3** as a function of pH, calculated from eq 8 assuming a pK_{a1} of 9.87 and a pK_{a2} of 12.4. Experimental conditions: pH 7.4−9.0 TRIS buffer, 9.5−11.5 CAPS buffer, buffer concentration 0.05 M, I = 0.15 M set with $NaClO_4$, [AcMP-11] = 2.5 × 10^{-6} M, T = 20 °C.

The NO dissociation rates (k_{off}) were measured with a NO-trapping method with the application of $[Ru^{III}(edta)Cl]^{2-}$ as a NO scavenger. Such an approach allowed more accurate data to be obtained (Table S5), since k_{off} values determined from the intercept of the fitted linear regression are susceptible to extrapolation errors. In aqueous solution, the $[Ru^{III}(edta)Cl]^{2-}$ complex rapidly aquates and produces $[Ru^{III}(edta)(H_2O)/(OH)]^{-/2-}$, which in turn rapidly traps NO, such that NO release from $[(AcMP\text{-}11)Fe^{II}(NO^+)(HisH)/(His^-)]$ becomes the rate-limiting step (k_{obs} = k_{off}; Scheme 2).[75]

https://doi.org/10.1021/acs.inorgchem.1c00933
Inorg. Chem. 2021, 60, 15948−15967

Scheme 2

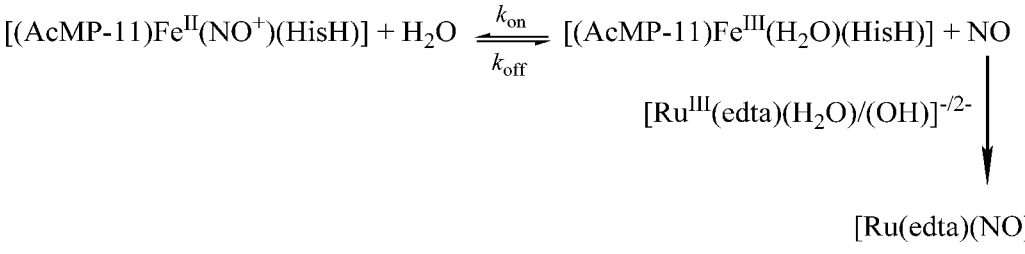

NO Binding Rate Constant (k_{on}). A monotonic decrease of the k_{on} value with pH is evident, and the shape of this dependence is consistent with the occurrence of two pH-dependent transformations of AcMP-11 in the pH range of 7–13, which is inferred from the pH-titration experiments, for both the results of Marques and Perry[35] and our own in Figure S8 (Supporting Information).

A quantitative interpretation of the dependence of k_{on} on pH in Figure 5 is complicated by the closeness of the pK_{a1} and pK_{a2} values. In general, the k_{on} value determined at a given pH includes contributions from all three pH-dependent AcMP-11 forms weighted by their molar fractions:

$$k_{on} = x_1 k_{on}^{(1)} + x_2 k_{on}^{(2)} + x_3 k_{on}^{(3)} \quad (8)$$

In eq 8, the molar fractions x_i are known functions of the pH expressed by eqs 9a–9c), whereas $k_{on}^{(i)}$ (i = **1**, **2**, **3**), the individual rate constants characterizing a given form of AcMP-11, are the pH-independent unknown parameters to be determined by fitting the above model to the experimental data.

$$x_1 = (1 + 10^{pH-pK_{a1}} + 10^{2\cdot pH-pK_{a1}-pK_{a2}})^{-1} \quad (9a)$$

$$x_2 = 10^{pH-pK_{a1}} \times x_1 \quad (9b)$$

$$x_3 = 10^{2\cdot pH-pK_{a1}-pK_{a2}} \times x_1 \quad (9c)$$

The experimental data (black dots, Figure 5a) were fitted with various approaches (see also Figure S9, Supporting Information). Initially, fixed values of pK_{a1} and pK_{a2} from the pH-titration reported by Marques and Perry[35] (which are also in good agreement with our own pH-titration measurements, see section Behavior of AcMP-11 in Alkaline Solution) were taken, and the function was fitted only with respect to the $k_{on}^{(1)}$, $k_{on}^{(2)}$, and $k_{on}^{(3)}$ parameters with the constraint that all of them must be non-negative. However, such an approach resulted in a poor fit quality (Figure S9). The quality of the fit can be considerably improved by adjusting the pK_{a1} value, leading to the fitting results shown in Figure 5a. Attempts to similarly adjust the pK_{a2} value did not significantly improve the quality of the fit, and the results obtained in such a way showed signs of overfitting problems (Figure S9) due to the limited number of data points at very high pH.

The value of pK_{a1} = 9.89 determined by fitting the kinetic data is higher by 0.3 units than the value determined from the spectrophotometric pH-titration (9.56 from ref 35 and 9.53 from a two-step transition model reported here Behavior of AcMP-11 in Alkaline Solution). The discrepancy is most probably the result of an aggregation process of AcMP-11 observed under alkaline conditions (see section Behavior of AcMP-11 in Alkaline Solution). The aggregation has a significant influence on the pK_{a1} value obtained from a pH-dependent titration but does not affect the value determined from kinetic studies, since by fitting a double-exponential function to the recorded kinetic traces (see above), our method of analysis separates the kinetic behavior of the monomers and aggregates. Concerning the pK_{a2} value, the pH dependence of the kinetic data in Figure 5a is in satisfactory agreement with the value determined from the spectrophotometric pH-titrations to within the uncertainties (12.4 from ref 35, 12.56 reported in this work). This is consistent with less pronounced aggregation at more alkaline pH values (see below).

Strikingly, the fitted results shown in Figure 5a, indicate that $k_{on}^{(3)}$ is zero (with a relatively large statistical error bar). We checked that identical $k_{on}^{(1)}$ and $k_{on}^{(2)}$ values are obtained by fixing $k_{on}^{(3)}$ = 0 and fitting only $k_{on}^{(1)}$ and $k_{on}^{(2)}$ (and optionally also pK_{a1}; see Figure S9). Attempts to fit all three $k_{on}^{(i)}$ values without the constraint of their non-negativity resulted in a slightly negative (therefore nonphysical) value of $k_{on}^{(3)}$, again with a relatively large statistical uncertainty. Taken together, these results are indicative of $k_{on}^{(3)}$ being zero to within the experimental uncertainty. In other words, our kinetic data reported in Figure 5 are consistent with the model defined in eq 8 in which *only forms **1** and **2** actively contribute to the NO binding kinetics observed in the studied pH range ($k_{on}^{(1)}$, $k_{on}^{(2)} > 0$), whereas form **3** is kinetically inert ($k_{on}^{(3)} \sim 0$; specifically, $k_{on}^{(3)} \ll k_{on}^{(2)}$).*

The values of $k_{on}^{(1)}$ and $k_{on}^{(2)}$ resulting from fitting eq 8 to the experimental data in Figure 5a are considerably independent of the way of treating the $k_{on}^{(3)}$ term (i.e., constrained to be non-negative, not constrained, or fixed to zero; see Figure S9). In all cases, the obtained value of $k_{on}^{(1)}$ is comparable to analogous values for ferric porphyrins with labile aqua ligands.[9,12,22] As could be expected, the $k_{on}^{(2)}$ is smaller than $k_{on}^{(1)}$, but remarkably, it is smaller by only 1 order of magnitude (i.e., $k_{on}^{(1)}/k_{on}^{(2)} \sim$ 10:1). Such a high ligand-exchange reactivity is unexpected for **2**, which was so far characterized as a six-coordinate metal–hydroxo complex. Taken together with the apparent inertness of form **3**, these findings are surprising enough to deserve a more detailed discussion in the context of the proposed reaction mechanism (see below).

NO Dissociation Rate Constant (k_{off}). In contrast to k_{on}, the determined values of k_{off} remained constant up to pH 11.5. The slight decrease of k_{off} was observed only above pH 11.5. Obtained results indicate no significant change in the rate constant for NO release on going from [(AcMP-11)-Fe^{II}(NO$^+$)(HisH)] to [(AcMP-11)Fe^{II}(NO$^+$)(His$^-$)], Figure 6. Previously, for numerous porphyrin systems, a decrease in the rate constant for NO binding (k_{on}) to [(Por)Fe^{III}(H$_2$O)$_2$] in comparison to [(Por)Fe^{III}(H$_2$O)(OH)] or [(Por)-Fe^{III}(OH)] and a significant decrease in the rate constant for the release of NO (k_{off}) were also observed.[14,18,76,77] This observation led to the conclusion that the lability of the iron center, which should be increased by a coordinated hydroxo group, does not control the complexity of the observed

https://doi.org/10.1021/acs.inorgchem.1c00933
Inorg. Chem. 2021, 60, 15948–15967

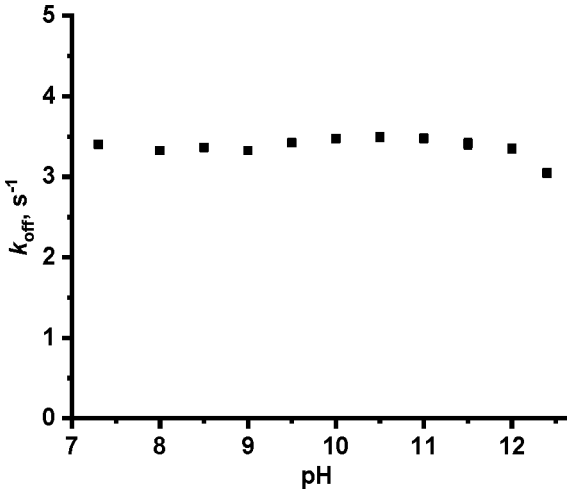

Figure 6. Dependence of k_{off} on pH for the fast reaction step of NO binding to AcMP-11. Experimental conditions: pH 7.4−8.0 phosphate buffer, 8.5−9.0 CHES buffer, 9.5−11.5 CAPS buffer, 12.0−12.4 NaOH, buffer concentration 0.025 M, I = 0.15 set with $NaClO_4$, $[Ru(edta)Cl]^{2-}$ = 0.5 mM, [AcMP-11] = 2×10^{-6} M, [NO] = 1.5×10^{-5} M, T = 20 °C.

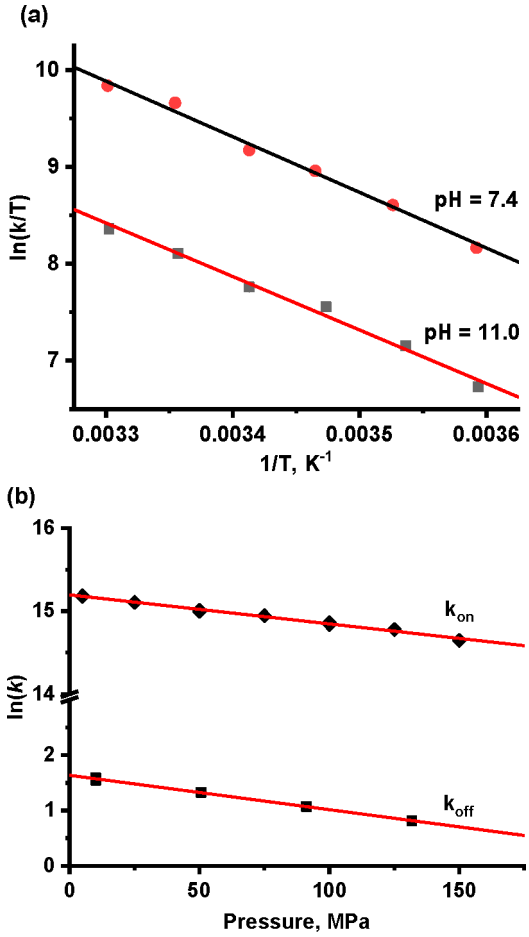

Figure 7. (a) Example of Eyring plots of $\ln(k_{on}/T)$ vs $1/T$ at pH 7.4 and 11.0. (b) Example of plots of $\ln(k_{on})$ and $\ln(k_{off})$ vs pressure. Experimental conditions: (a) [AcMP-11] = 2×10^{-6} M, [NO] = 5×10^{-5} M, pH 7.4, 0.05 M phosphate buffer; pH 11, 0.05 M CAPS buffer, I = 0.15 M ($NaClO_4$). (b) k_{on}: [AcMP-11] = 5×10^{-6} M, [NO] = 7.5×10^{-4} M, pH 7.4, 0.05 M Tris buffer, I = 0.15 M ($NaClO_4$), T = 20 °C. k_{off}: [AcMP-11] = 2×10^{-6} M, [NO] = 1.5×10^{-5} M, $[Ru(edta)Cl]^{2-}$ = 0.5 mM, 0.05 M Tris buffer, I = 0.15 M ($NaClO_4$), T = 25 °C.

reactivity. The pH-dependent decrease in the rate was assigned to a much higher activation barrier resulting from the overall spin state change and structural reorganization on NO binding to the aqua vs hydroxo form and, analogously, NO release from $[(Por)Fe^{II}(NO^+)(H_2O)]$ and $[(Por)Fe^{II}(NO^+)(OH)]$, respectively.[18]

Therefore, the lack of a meaningful influence of pH in the range up to 11.5 on the k_{off} value for denitrosylation of AcMP-11, suggests that no significant difference in spin and structure reorganization occurs for NO release from these two species $[(AcMP\text{-}11)Fe^{II}(NO^+)(HisH)]$ vs $[(AcMP\text{-}11)Fe^{II}(NO^+)(His^-)]$. Knowing that the k_{off} value represents the transformation of the six-coordinate nitrosyl species $[(AcMP\text{-}11)Fe^{II}(NO^+)(HisH)]/[(AcMP\text{-}11)Fe^{II}(NO^+)(His^-)]$ to a five-coordinate intermediate $[(AcMP\text{-}11)Fe^{III}(HisH)]/[(AcMP\text{-}11)Fe^{III}(His^-)]$ (both species having the same high spin state), a lack of the influence of histidine deprotonation on the k_{off} value is understandable (see further discussion based on theoretical calculations).

Activation Parameters. To take a closer look at the mechanism of NO binding by AcMP-11, the k_{on} and k_{off} values were determined as a function of temperature and hydrostatic pressure at selected pH values. The resulting activation parameters are presented in Table 1, whereas Eyring plots of $\ln(k_{on}/T)$ vs $1/T$ at pH 7.4 and 11.0, as well as plots of $\ln(k_{on})$ and $\ln(k_{off})$ vs pressure, are presented in Figure 7a and b. Unfortunately, we were only able to determine the $\Delta V^{\ddagger}$ at pH 7.4. Measurements of k_{on} and k_{off} as a function of pressure under alkaline conditions were impossible due to the occurrence of reductive nitrosylation, which prevented high pressure laser flash photolysis measurements for k_{on} (reaction was too fast to apply high-pressure stopped flow) and application of the NO-trapping method for k_{off}, since they require preparation of nitrosylated AcMP-11, which is unstable under alkaline conditions.

Table 1. Rate Constants and Activation Parameters for Reversible Binding of NO to AcMP-11 at Selected pH Values Determined by Laser Flash Photolysis,[a] Stopped-Flow, and NO-Trapping Method (k_{off})

	NO binding					NO release	
pH	7.4		9.5	10.0	11.0	7.4	11.0
k at 20 °C	3.3×10^{6}[b,c]	3.8×10^{6}[b]	2.8×10^{6}[b]	1.7×10^{6}[b]	0.6×10^{6}[b]	3.4[c]	3.5[c]
$\Delta H^{\ddagger}$ (kJ/mol)	49 ± 2[a]	50 ± 2	47 ± 2	44 ± 2	46 ± 2	94 ± 1	87 ± 5
$\Delta S^{\ddagger}$ (J/mol K)	+48 ± 3[a]	+48 ± 4	+41 ± 8	+27 ± 7	+24 ± 7	+85 ± 3	+62 ± 17
$\Delta V^{\ddagger}$ (cm^3/mol)	+8.6 ± 0.4[a]					+15.4 ± 0.4	

[a]From laser flash photolysis. [b]k_{on} in M^{-1} s^{-1}. [c]k_{off} in s^{-1}.

https://doi.org/10.1021/acs.inorgchem.1c00933
Inorg. Chem. 2021, 60, 15948−15967

As can be seen from the obtained data, positive values of $\Delta S^{\ddagger}$ under neutral and alkaline conditions, as well as a more diagnostic positive value of $\Delta V^{\ddagger}$ obtained at pH 7.4, point toward a dissociative ligand substitution mechanism over the whole studied pH range. This is in agreement with earlier mechanistic studies on NO binding to six-coordinate diaqua ligated iron(III) porphyrins, which show that the rate of NO binding in $(Por)Fe^{III}(H_2O)_2$ species is controlled by a rate-limiting water dissociation.[20,21] Positive values of $\Delta S^{\ddagger}$ obtained at pH 9.5−11.0 support the six-coordinate nature of form **2** of AcMP-11.

Reaction Mechanism. *Controversies.* The above discussion of the pH-dependent reactivity of AcMP-11 toward NO (Figure 5) puts to the test our current understanding of ligand-exchange mechanisms in metalloporphyrins. In particular, the finding that form **2**, characterized in the literature as six-coordinate hydroxo complex **2a**,[35] binds NO only ∼10 times slower than form **1**, characterized as a six-coordinate aqua complex, is surprising in view of the expectation that the Fe−OH bond in **2a** should be inert due to its much higher bond energy when compared with the $Fe-OH_2$ bond in **1**, leading to a pronounced decrease in the k_{on} value. One can obtain a rough idea of how much the Fe−OH bond (in **2a**) is stronger than the $Fe-OH_2$ bond (in **1**) from a simple thermochemical cycle (Figure S10, Supporting Information) that considers the dissociation of both bonds and the acid−base equilibria between **1** and **2a** and between H_2O and OH^-. This leads to the following estimate of the difference between the Gibbs free energies of breaking the Fe−OH bond in **2a** and the $Fe-OH_2$ bond in **1**

$$\begin{aligned}&\Delta G(\mathrm{Fe-OH}) - \Delta G(\mathrm{Fe-OH_2})\\ &= (\mathrm{p}K_{\mathrm{H_2O/OH^-}} - \mathrm{p}K_{\mathrm{a1}}) \times RT \ln 10\\ &\approx 35\ \mathrm{kJ/mol}\end{aligned} \tag{10}$$

where pK_{a1} = 9.6 and pK_{aH_2O/OH^-} = 15.7 are the negative logarithms of the acidity constants of AcMP-11 (**1** ⇔ **2**) and water, respectively. The use of pK_{a1} value 9.9 determined from the kinetic analysis (see above, Figure 5) leads to an estimate of 33 kJ/mol. If the above estimated difference between the $Fe-OH_2$/OH bond strengths (33−35 kJ/mol) governed the rates of NO binding to forms **1** and **2**, one would obtain a 10^5- to 10^6-fold decrease of the rate constant for form **2** compared to form **1**, rather than the actually observed decrease by a factor of only 10.

The expectation that the metal−hydroxo bond should be inert in ligand substitution reactions is strongly supported by the available kinetic studies of six-coordinate metalloporphyrins whose pH-dependent forms have $(H_2O)_2$, $(H_2O)(OH)$, and $(OH)_2$ as axial ligands; of these, only the first two forms, which have labile metal−OH_2 bonds, contribute to the observed ligand substitution rates.[78−80] Within a broader context of coordination chemistry, it is possible to find only rare reports of metal−hydroxyl bonds being comparably reactive in ligand substitution as metal−aqua bonds, such as in the reaction of $[Mo(O)(OH)(CN)_4]^{3-}$ with 1,10-phenanthroline[81] and for some other reactions of cyanido complexes mentioned in ref 81. However, later re-examination of the same tetracyanomolybdate reacting with the related bidentate ligand (2,2′-bipyridine) revealed that, in accord with chemical intuition, the aqua form $[Mo(O)(OH_2)(CN)_4]^{2-}$ is "practically the only reactive species,"[82] and the same regular behavior was observed in the reactivity of the analogous tetracyanotungstate complex with the 2-pyridinecarboxylate ligand.[83] These cyanido-based complexes for which anomalously high OH^- exchange rates were suggested could react under an associative mechanism, such that cleavage of a strong metal−OH bond is no longer the rate-limiting step. However, the analogous mechanism is improbable in the case of six-coordinate porphyrin complexes, and actually for the present case of AcMP-11, it can be ruled out by the measured activation parameters—indicative of the usual dissociative mechanism over the whole pH range studied (see above).

The second unexpected observation of our findings is the inertness of the hydroxo complex with deprotonated histidine (form **3**). Marques et al.,[45] in one of their articles concerned with kinetic studies on the MP-8 reactivity with CN^-, concluded that the microperoxidase OH^- form is inert, whereas ionization of HisH, related with the increase in charge density on this ligand present in the *trans* position to the OH^- group, results in the labilization of the Fe−OH bond in form **3**.[36] We certainly agree that the mentioned *trans* effect operates here, i.e., deprotonation of HisH elongates the Fe−OH bond *trans* to it and reduces the bond energy (see DFT geometries and bond energies compared in Figure S11, Supporting Information). However, the Fe−OH bond remains very strong compared with the corresponding $Fe-OH_2$ bond (Figure S11), conforming to the present experimental observations that this labilization of OH^- by the His^- ligand in the *trans* position has no "positive" effect on the reactivity of form **3** in comparison to form **2**; in fact, exactly the opposite is observed.

As a side remark, we noticed that the binding of HCN/CN^- to MP-8 studied in ref 45 is noticeably more complicated than the presently studied binding of NO to AcMP-11, and these complications may influence the validity of the conclusions obtained in that study. The main complication (which is not present in our system) is the protonation of CN^- occurring with $pK_{a(HCN)}$ = 9.9 that is close to the pK_{a1} = 8.9 value of MP-8 (**1** ⇔ **2** transformation) and to the pK_{a2} = 10.5 (**2** ⇔ **3**). (Note that for MP-8, these pK_a values are different than for the presently studied AcMP-11). Thus, for the reaction of HCN/CN^- with MP-8 considered in ref 45, there are three deprotonations that occur in the relatively narrow pH range of 9−11. Another complication might be a higher tendency of (unacetylated) MP-8 to aggregate compared to the present case of (*N*-acetylated) AcMP-11. In fact, even for AcMP-11 in the micromolar concentration range, we found the dimerization process to be relevant in the alkaline pH near pK_{a1} and accounted for this in our analysis of kinetic data (see above) by separating the reactivity of the monomer from the slow component related to the reactivity of the dimer. Finally, we would like to point out that the conclusions reached in the kinetic study of CN^- binding to MP-8 in ref 10 appear to be problematic in view of our presented data. This concerns the notion that form **2** of MP-8 does not contribute to the overall reactivity. The only assumption made in eq 8 is that there are three acid−base forms of AcMP-11 coexisting in the studied pH range that all contribute to the experimental k_{on} value, proportionally to their molar fractions and their acid−base equilibria, which control the molar fractions, to settle fast enough not to be rate-limiting steps. Similar assumptions are also made in the kinetic model of ref 45. The common assumption that acid−base equilibria settle fast enough not to be rate-limiting steps is a result of the buffer being present in a

https://doi.org/10.1021/acs.inorgchem.1c00933
Inorg. Chem. 2021, 60, 15948−15967

large excess to stabilize the pH, and at the same time, it acts as a potent reservoir and acceptor of protons.

Thus, our observation that labilization of the OH^- by deprotonation of the *trans* histidine *does not* make form **3** of AcMP-11 active toward ligand binding, taken together with the fact that form **2** of AcMP-11 binds the ligand unexpectedly fast, proves that other processes rather than rate-limiting OH^- dissociation govern the reactivity of the alkaline forms **2** and **3** of AcMP-11 toward NO binding. At first sight, the high reactivity of form **2** observed by us may seem to be consistent with the proposal of van Wart and co-workers that form **2** of microperoxidase is mainly a five-coordinate complex with deprotonated histidine,[84] rather than a six-coordinate complex **2a** (as assumed so far). However, the positive values of $\Delta S^{\ddagger}$ obtained at pH 9.5−11.0 (see above) support the six-coordinate nature of form **2** of AcMP-11 and hence the dissociative mechanism. Moreover, the detailed analyses of UV−vis spectra of various microperoxidases, including AcMP-11, performed in the Marques group,[35,36] provide compelling evidence that form **2** must be dominated by a six-coordinate complex.

Below, we present a mechanism that can account for all the observed effects. By performing quantum-chemical calculations, we show it to be qualitatively in good agreement with the experimental data. The mechanism is still dissociative in nature, but it accounts for the surprising high reactivity of form **2** by introducing the possibility of a tautomerization reaction which was not considered up to now in mechanistic studies of microperoxidases. The five-coordinate complex proposed by van Wart and co-workers[84] is important to account for the unexpected high reactivity of AcMP-11, although our calculations confirm that it is not the main molecular species present under alkaline conditions.

Proposed Reaction Mechanism. As discussed above, three acid/base forms of microperoxidase (**1**, **2**, **3**) are relevant in the studied pH range. The reactivity of form **1**, the [(AcMP-11)$Fe^{III}(H_2O)$(HisH)] complex, is ascribed to the dissociation of its H_2O axial ligand, leading to the transient formation of a five-coordinate complex (**A**), which is the NO binding target (Scheme 3). This is the standard dissociative mechanism, well established for analogous water-ligated ferric porphyrins.[9,20,22]

Under the steady-state approximation with respect to transient **A**, with the realistic assumption that $k_{-1}[H_2O] \gg k_A[NO]$, because under the experimental conditions $[H_2O] \gg [NO]$, the effective second-order rate constant of NO binding to form **1** of microperoxidase reads[22]

$$k_{on}^{(1)} = \frac{k_1 k_A}{k_{-1}[H_2O]} = \frac{K_1}{[H_2O]} k_A \qquad (11)$$

where $K_1 = k_1/k_{-1}$ is the equilibrium constant for water dissociation from **1**.

In the singly deprotonated form of microperoxidase (**2**), the main molecular species is the six-coordinate complex [(AcMP-11)Fe^{III}(OH)(HisH)] (**2a**). As was discussed above, the Fe−OH bond is expected to be inert, which is in contrast to the relatively fast kinetics of the reaction of **2** with NO observed experimentally (see above). In order to explain this paradox, we propose that there exists a tautomeric equilibrium between [(AcMP-11)Fe^{III}(OH)(HisH)] (**2a**) and [(AcMP-11)-$Fe^{III}(H_2O)(His^-)$] (**2b**), as illustrated in Scheme 4. Although tautomer **2b** is less stable than **2a** (see further results), it has a labile Fe−OH_2 bond and hence can release the H_2O ligand to produce the five-coordinate complex (**B**), which is the NO binding target. The initially formed nitrosyl product will thus be [(AcMP-11)$Fe^{II}(NO^+)(His^-)$] (**Y**); depending on the pH, it may subsequently protonate to [(AcMP-11)$Fe^{II}(NO^+)$-(HisH)] (**X**). Note that the experimental $pK_{a(NO)}$ value of the [(AcMP-11)$Fe^{II}(NO^+)$(HisH/His^-)] pair is larger by more than one unit than that of the [(AcMP-11)$Fe^{III}(H_2O$/OH)(HisH)] pair (Scheme 1). The proposed mechanism is shown in Scheme 4.

Analogously as derived above for species **1** (again, assuming $k_{-2}[H_2O] \gg k_{-B}[NO]$ and also that the tautomeric equilibrium and acid base equilibrium settle fast), the effective second-order rate constant for NO binding to form **2** of microperoxidase reads

$$k_{on}^{(2)} = \frac{K_2}{[H_2O]} \frac{K_t}{(1 + K_t)} k_B \approx \frac{K_2 K_t}{[H_2O]} k_B \qquad (12)$$

where K_t is the tautomerization equilibrium constant and $K_2 = k_2/k_{-2}$ is the equilibrium constant for water dissociation from **2b**. The factor $K_t/(1 + K_t)$ accounts for the fraction of reactive tautomer **2b** in form **2** being the mixture of both tautomers. The second form of eq 12 is valid if $K_t \ll 1$.

Finally, form **3** of microperoxidase (doubly deprotonated with respect to **1**) is the six-coordinate complex [(AcMP-11)Fe^{III}(OH)(His^-)], which has an inert Fe−OH bond, and

Scheme 3. Dissociative Mechanism of NO Reaction with Form 1 of Microperoxidase

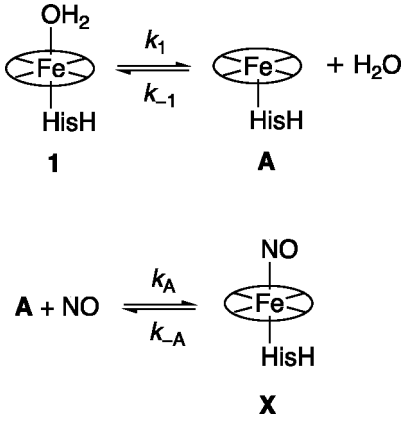

Scheme 4. Dissociative Mechanism (with Tautomerization) Proposed for the Reaction of NO with Form 2 of Microperoxidase

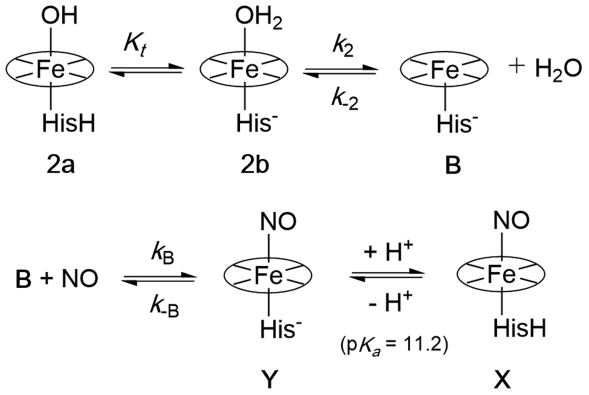

https://doi.org/10.1021/acs.inorgchem.1c00933
Inorg. Chem. 2021, 60, 15948−15967

by contrast with **2a**, it cannot tautomerize to labile Fe−OH_2 species because the histidine (and any other viable proton source in this molecule) is deprotonated. Therefore, complex **3** is inert under the dissociative mechanism, which is exactly what the experimental data show: $k_{on}^{(3)} \approx 0$ within the data uncertainty (see above).

Computational Evaluation of Proposed Mechanism. The mechanism proposed in the previous section automatically explains the experimental observation that form **3** is practically inert toward the reaction with NO. Whether or not this mechanism can also account for the observed relatively fast kinetics of the NO reaction with form **2** as compared to form **1** depends on actual values of the thermodynamic (K_1, K_2, K_t) and kinetic (k_A, k_B) quantities underlying $k_{on}^{(1)}$ and $k_{on}^{(2)}$. Based on eqs 11 and 12, the ratio of the two effective rate constants for NO binding may be viewed as a product of two factors [eq 13]

$$\frac{k_{on}^{(2)}}{k_{on}^{(1)}} = \frac{k_B}{k_A} \times \frac{K_t K_2}{K_1} \tag{13}$$

The first factor is the ratio of the elementary rate constants for NO binding to transient, five-coordinate species **A** and **B**. The second factor is the ratio of the equilibrium constants, which measures the *relative lability* of the axial ligand in **1** and **2**: it compares the free energy required for converting hydroxo complex **2a** (predominant tautomer of **2**) into aqua complex **2b**, and then into reactive **B** (by water dissociation), with the free energy required for directly converting aqua complex **1** into reactive **A**. It is convenient to operate with the negative logarithm of this relative lability factor, i.e. the ΔpK quantity defined as

$$\Delta pK \equiv -\log\left(\frac{K_t K_2}{K_1}\right) = pK_t + pK_2 - pK_1 \tag{14}$$

We performed quantum chemical calculations to determine the pK_i values in eq 14 from the standard Gibbs free energies of the respective reactions (water dissociations from **1** and **2b** in the case of $pK_{1,2}$; tautomerization of **2a** into **2b** in the case of pK_t) and making use of the fact that

$$pK_i \equiv -\log K_i = \gamma \Delta G_i \tag{15}$$

where $\gamma = (RT \ln 10)^{-1}$, $i = 1, 2, t$.

All further considerations in this section rely on having established accurate spin-state energetics with the aid of the DFT+ΔCC approach, which is detailed below in the section Spin-State Energetics of AcMP-11. The thermochemical functions (ΔG, ΔH) and resulting pK values reported below are spin-unresolved ones, based on DFT reaction energies computed assuming fixed HS state for all Fe^{III} complexes (to minimize DFT-related errors) and later corrected, based on reliable DFT+ΔCC spin-state energetics, to reflect thermal equilibria between all three spin states [see Computational Methods and Models, eqs 3−5). We found this approach necessary in order to obtain physically reasonable values, in particular, to avoid artifacts—related to incorrect prediction of the lowest spin state or unbalanced energies for reactions involving the change of spin state (even when the correct spin states are assumed)—which would appear otherwise at the uncorrected DFT level. This approach also significantly reduces the sensitivity of the obtained results to the choice of DFT functional. Below, only results obtained with B3LYP-D3 and M06L functionals are shown (in combination with the PCM and SMD solvation), whereas additional B3LYP*-D3 and TPSSh-D3 results can be found in the Supporting Information.

Water Dissociation Constants. Table 2 reports the computed enthalpies (ΔH_1, ΔH_2), free energies (ΔG_1, ΔG_2), and the corresponding pK values (pK_1, pK_2) describing the dissociations of the water ligand from aqua complexes **1** and **2b**. It can be seen that the SMD solvation model predicts much lower ΔH and ΔG values than the PCM model, and there is also some small variation of these values with the choice of DFT method (see full set of results in Table S6, Supporting Information). However, both solvation models and all four tested DFT methods agree that the Fe−OH_2 binding strength is reduced (in terms of ΔG) by about 5−9 kJ/mol in **2b** with respect to **1**, corresponding to the reduction in the pK values by 1−1.5 log units. This is a manifestation of the *trans* labilizing effect of the His^- ligand.

Table 2. Computed Enthalpies, Gibbs Free Energies, and pK Values of Water Dissociation from Species 1 and 2b[a,b]

	PCM model		SMD model	
	B3LYP-D3 (+ΔCC)	M06L (+ΔCC)	B3LYP-D3 (+ΔCC)	M06L (+ΔCC)
ΔH_1	42.5	49.4	18.5	21.4
ΔH_2	32.0	44.3	10.8	13.3
ΔG_1	30.8	34.8	6.9	11.4
ΔG_2	22.7	27.0	1.6	5.2
pK_1	5.4	5.8	1.2	2.0
pK_2	4.0	4.4	0.3	0.9

[a] ΔH_i and ΔG_i values in kJ/mol, pK_i dimensionless. [b] Thermochemical functions were obtained by combining the DFT results in the HS channel (Table S3) with the "ensemble corrections" at the DFT +ΔCC level (Table S4); see Supporting Information.

Interestingly, the Fe−OH_2 bond enthalpy of complex **1** (ΔH_1 of 42−49 kJ mol^{-1}) obtained with the PCM model and the corresponding entropy change (ΔS_1 of 39−48 J K^{-1} mol^{-1}, calculated from ΔH_1 and ΔG_1) appear to be in reasonably good agreement with the experimental activation parameters at pH 7.4 (where species **1** is predominant): $\Delta H^{\ddagger}$ of about 50 kJ mol^{-1} and $\Delta S^{\ddagger}$ of 48 J K^{-1} mol^{-1} (Table 1). Obviously, one should not expect the computed bond breaking parameters (ΔH_1, ΔS_1) to exactly reproduce the experimental activation parameters ($\Delta H^{\ddagger}$, $\Delta S^{\ddagger}$) because—even for a purely dissociative mechanism—the latter quantities, especially $\Delta S^{\ddagger}$, should also contain some information on the spin-forbidden NO binding step to **A** (Scheme 3), which is not explicitly modeled here. The other reason is the lack of full separation between the enthalpy and free energy when using an implicit solvation model, like PCM. Nonetheless, a reasonably good match between the calculated Fe−OH_2 bond breaking parameters of **1** and the experimental activation parameters at pH 7.4 shows that the former values are realistically described by our computational protocol.

Tautomerization Constant and Acidity Constants. Table 3 reports the computed enthalpy (ΔH_t), free energy (ΔG_t), and the corresponding pK_t values that describe the tautomerization of hydroxo complex **2a** into aqua complex **2b**. The calculated values have some dependence on the choice of DFT method and solvation model (see also full set of results in Table S7,

https://doi.org/10.1021/acs.inorgchem.1c00933
Inorg. Chem. 2021, 60, 15948−15967

Table 3. Computed Enthalpy, Gibbs Free Energy, and Directly Computed Tautomerization Constant (pK_t)[a,b]

	PCM model		SMD model	
	B3LYP-D3 (+ΔCC)	M06L (+ΔCC)	B3LYP-D3 (+ΔCC)	M06L (+ΔCC)
ΔH_t	39.0	24.7	24.0	20.7
ΔG_t	21.0	16.3	18.2	14.2
pK_t[c]	3.7	2.8	3.2	2.5

[a] ΔH_t and ΔG_t values in kJ/mol, pK_t dimensionless. [b] Thermochemical functions were obtained by combining the DFT results in the HS channel (Table S3) with the "ensemble corrections" at the DFT +ΔCC level (Table S4); see Supporting Information. [c] Directly calculated from ΔG_t using eq 15.

Supporting Information), but all of them confirm that tautomerization of **2a** into **2b** is endothermic and endergonic.

The directly computed $pK_t \approx 3$ would be indicative of only one **2b** molecule for 1000 molecules of **2a**. However, the reliability of the directly computed tautomerization constant relies on the ability of the computational protocol to correctly reproduce relative acidities of the H_2O/OH^- and $HisH/His^-$ ligands in ferric AcMP-11. We thus calculated and compared with the experimental values the pK_a values describing deprotonation of form **1** into **2** (pK_{a1}), form **2** into **3** (pK_{a2}), and nitrosyl species **X** into **Y**. Because form **2** is not pure **2a**, but also contains tautomer **2b**, in principle, one should distinguish between the macroscopic (pK_{a1}, pK_{a2}) and microscopic ($pK_{a1/2a}$, $pK_{a2a/3}$) acidity constants,[72] leading to the following exact relationships:

$$pK_{a1} = pK_{a1/2a} - \log(1 + 10^{-pK_t}) \quad (16a)$$

$$pK_{a2} = pK_{a2a/3} + \log(1 + 10^{-pK_t}) \quad (16b)$$

In practice, the approximations $pK_{a1} \approx pK_{a1/2a}$ and $pK_{a2} \approx pK_{a2a/3}$ are justified when comparing the calculated values with experimental ones (the resulting error is within 0.1 log unit if $pK_t > 0.6$ and even for the extreme case of $pK_t = 0$, it will be a tolerable 0.3 log unit). Table 4 reports the pK_a values

Table 4. Calculated and Experimental pK_a Values

	calcd B3LYP-D3(+ΔCC)				
	PCM, direct[a]	SMD, direct[a]	PCM, PE[b]	SMD, PE[b]	exptl
$pK_{a1/2a}$	7.5	9.4	9.1	11.6	9.6[c]
$pK_{a2a/3}$	13.6	14.4	14.0	14.8	12.4[c]
$pK_{aX/Y}$	11.8	13.2	12.2	13.6	11.2[d]
$pK_{a\ H_2O/OH^-}$	14.1	13.5	e	e	15.7
$pK_{a\ ImH/Im^-}$	14.0	14.0	e	e	14.4[f]

[a] Direct method. [b] Proton exchange (PE) method taking H_2O/OH^- as the reference for **1**/**2a** and ImH/Im^- as the reference for **2a**/**3** and **X**/**Y**. [c] Ref 35 (pK_{a1} and pK_{a2} in Scheme 1). [d] This work ($pK_{a(NO)}$ in Scheme 1). [e] In the PE method these values are by construction equalized to experimental ones. [f] Ref 85.

computed using the direct approach and proton exchange (PE) method, based on experimental pK_a's of free water (H_2O/OH^-) and imidazole (ImH/Im^-). Only the B3LYP-D3-(+ΔCC) results are shown here (in combination with PCM and SMD solvation models), whereas the full set of results can be found in Table S8, Supporting Information.

All applied methods (see also Table S8) qualitatively recover the experimental trend that $pK_{a1/2a} < pK_{aX/Y} < pK_{a2a/3}$, i.e., the H_2O ligand in **1** deprotonates more easily than the HisH ligand in species **X**, and the latter one still more easily than the HisH ligand in species **2**. In quantitative terms, however, the calculated pK_a values are not perfect, and in particular they reveal the following important shortcoming: the difference between any of the pK_a's related to deprotonation of HisH ($pK_{a2a/3}$ and $pK_{aX/Y}$) and that related to deprotonation of H_2O ($pK_{a1/2a}$) is *significantly overestimated with respect to the experiment*, particularly by the direct method (by up to 3.3 log units) and slightly less by the PE method (usually by not more than 2 log units). The appearance of such errors in DFT-computed pK_a's is not unusual,[86−88] especially with regard to computationally challenging acidities of ligands in transition metal complexes[89−95] and when comparing the computed pK_a's for protic groups with considerably different chemical character (like here, H_2O vs HisH).

It is vital to recognize that these imperfections of the computational protocol (most likely related to the solvation description), which lead to the error in relative pK_a values of H_2O and HisH ligands, translate into a systematic error of the directly computed tautomerization constant. Such a notion should be clear already by chemical intuition but can be put on firm ground with the aid of the thermochemical cycles shown in Scheme 5, allowing the derivation of the following two

Scheme 5. Relations between Microscopic Acidity Constants and Tautomerization Constant [Red (Blue) Arrows: Deprotonations of the H_2O (HisH) Ligand]

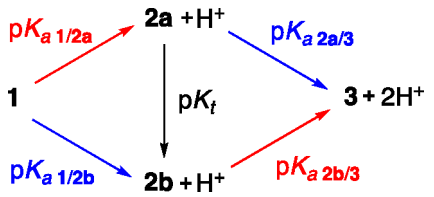

(equivalent) expressions which relate the pK_t to the microscopic pK_a's of which one ($pK_{a1/2a}$ or $pK_{a2b/3}$) describes deprotonation of the H_2O; the other ($pK_{a1/2b}$ or $pK_{a2a/3}$) describes deprotonation of the HisH ligand:

$$pK_t = pK_{a\,1/2b} - pK_{a\,1/2a} \quad (17a)$$

$$pK_t = pK_{a\,2a/3} - pK_{a\,2b/3} \quad (17b)$$

Although one of the microscopic acidity constants ($pK_{a1/2b}$ or $pK_{a2b/3}$) appearing in any one of the two relations given in eqs 17a, 17b) is not measurable in the experiment, the above experience with the measurable pK_a values suggests that the directly computed pK_a's related to deprotonation of H_2O are too low compared to those related to deprotonation of HisH, which results in the occurrence of a systematic error in the directly computed tautomerization constant (pK_t^{direct}): the H_2O ligand is predicted to deprotonate too easily compared to the HisH ligand! The systematic error in the directly computed tautomerization constant can be reduced by the PE scheme in which experimental pK_a's are used as the reference for describing the microscopic pK_a's in eq 17. One possibility is to refer to the experimental pK_a's of free ligands: ImH for the $pK_{a1/2b}$ and $pK_{a2a/3}$ and H_2O for the $pK_{a1/2a}$ and $pK_{a2b/3}$. This results in the following PE-corrected estimate of the pK_t:

https://doi.org/10.1021/acs.inorgchem.1c00933
Inorg. Chem. 2021, 60, 15948−15967

$$pK_t^{PE} = pK_t^{direct} + (pK_{a\,ImH/Im^-}^{exptl} - pK_{a\,H_2O/OH^-}^{exptl}) - (pK_{a\,ImH/Im^-}^{direct} - pK_{a\,H_2O/OH^-}^{direct}) \quad (18)$$

where pK_t^{direct} is the directly computed value (in Table 3). However, due to limited similarity of the free ligands (ImH/Im^- and H_2O/OH^-) to the ligands bound to Fe^{III} AcMP-11, this approach is not expected to fully compensate for the mentioned systematic error (for the same reason it *does not* work perfectly for the pK_a values of AcMP-11; cf Tables 4 and S8). We thus propose to use the PE scheme with an appropriately chosen "internal reference" that can best describe the acidic properties of H_2O and HisH ligands in AcMP-11, namely, to pick the "experimental" $pK_{a1/2a}$ as the reference for computing the $pK_{a2b/3}$ (both are related to deprotonation of the H_2O ligand) and the "experimental" $pK_{a2a/3}$ as the reference for computing the $pK_{a1/2b}$ (both are related to deprotonation of the HisH ligand). The reference values for the microscopic acidities $pK_{a1/2a}$ and $pK_{a2a/3}$ are close enough in practice to the experimental pK_{a1} and pK_{a2} values (see above). This PE scheme with the "internal reference" (int-PE) leads to the following corrected estimate of the tautomerization constant (the equation is derived in the Supporting Information):

$$pK_t^{int\text{-}PE} = pK_t^{direct} + (pK_{a2}^{exptl} - pK_{a1}^{exptl}) - (pK_{a\,2a/3}^{direct} - pK_{a\,1/2a}^{direct}) \quad (19)$$

Since the correction terms introduced in eqs 18 and 19 are on the order of 1−3 log units (Tables 4 and S8) and are usually negative, the resulting corrected pK_t values will be smaller than the directly computed ones (i.e., the tautomerization of **2a** into **2b** is more facile than it would seem to be from the raw computed data in Table 3). The implications of these considerations for our understanding of the reactivity of microperoxidase are discussed below.

*Relative Lability of Axial Ligand in Forms **1** and **2**.* We are now in a good position to discuss the relative lability of axial ligands in forms **1** and **2** of microperoxidase—in the sense of the ΔpK quantity defined earlier in eq 14. There are two contributions to the ΔpK value: (1) the $pK_2 - pK_1$ term describing the difference in water binding strengths between the aqua complexes (**2b** vs **1**) and (2) the pK_t term related to the free energy required for the tautomerization (**2a** into **2b**). Whereas the first term benefits from error cancelation and thus its current computational estimates are expected to be reliable, the second term suffers from systematic errors in the computed relative acidities of H_2O and HisH ligands in AcMP-11 (see above). To overcome this problem, we introduced, above, two empirically corrected estimates of the pK_t term, which are based on the PE (proton-exchange) method with the reference experimental pK_a values of either free H_2O and ImH ligands (pK_t^{PE}) or these ligands in ferric AcMP-11 ($pK_t^{int\text{-}PE}$). Table 5 reports all three estimates of the pK_t term (pK_t^{direct}, pK_t^{PE}, $pK_t^{int\text{-}PE}$) and the resulting estimates of the ΔpK quantity (ΔpK^{direct}, ΔpK^{PE}, and $\Delta pK^{int\text{-}PE}$; depending on how the problematic pK_t term is treated).

As discussed above, the directly computed pK_t values (2.7−3.7) are overestimated and hence point to the ΔpK^{direct} values that are too large (1.5−2.4) to explain the experimentally observed 10-fold decrease in the NO binding rate between forms **2** and **1**. However, this is a consequence of the above diagnosed imperfection in the present computational protocol,

Table 5. Computed difference in Fe−OH_2 Binding Strengths Between 2b and 1 ($pK_2 - pK_1$), Estimates of Tautomerization Constant (pK_t^{direct}, pK_t^{PE}, $pK_t^{int\text{-}PE}$) and Corresponding Estimates of ΔpK Quantity[a]

	PCM model		SMD model	
	B3LYP-D3 (+ΔCC)	M06L (+ΔCC)	B3LYP-D3 (+ΔCC)	M06L (+ΔCC)
$pK_2 - pK_1$[b]	−1.4	−1.4	−0.9	−1.1
pK_t^{direct}[c]	3.7	2.8	3.2	2.5
pK_t^{PE}[d]	2.5	3.4	1.4	2.5
$pK_t^{int\text{-}PE}$[e]	0.4	0.4	1.0	1.2
ΔpK^{direct}[f]	2.3	1.5	2.2	1.4
ΔpK^{PE}[f]	1.1	2.0	0.5	1.4
$\Delta pK^{int\text{-}PE}$[f]	−1.0	−1.0	0.1	0.1

[a]For full set of results, see Table S9, Supporting Information. [b]Data from Table 2. [c]Data from Table 3. [d]Corrected using the PE method based on experimental and computed pK_a's of H_2O/OH^- and ImH/Im^- (eq 18, data from Table 4). [e]Corrected using the PE method with internal reference (int-PE), i.e., based on experimental and computed pK_a's of AcMP-11 (eq 19, data from Table 4). [f]From eq 14, using either the direct, the PE, or the int-PE estimate of the pK_t term.

resulting in the overestimation of the acidity of the H_2O ligand relative to the HisH ligand, in turn resulting in the pK_t^{direct} values being too large, i.e., predicting the tautomerization being more endergonic than it actually is. The empirically corrected pK_t values (pK_t^{PE} and $pK_t^{int\text{-}PE}$) go qualitatively in the correct direction to compensate for this error. Specifically, they point (especially the int-PE estimates) to much lower pK_t values (larger amount of **2b** in phase **2**) and accordingly to the ΔpK quantity being much lower than that directly computed.

Due to the limited accuracy of the computed quantities and approximate character of the empirical corrections applied to the pK_t term, we do not have full confidence in the exact numeric values presented in Table 5. However, the following conclusions seem to be justified:

(1) The water ligand is labilized, by at least 1 order of magnitude, in tautomer **2b** as compared to the aqua complex **1**. This is due to the *trans* effect of His^-, as discussed before.

(2) Form **2** of AcMP-11 contains a molar fraction of tautomer **2b**, which is definitely larger than that predicted by the direct free energy computation (within the present computational protocol). It is currently impossible to determine this molar fraction exactly due to the uncertainty in the pK_t term. For instance, the int-PE estimates of the pK_t fluctuate between 1.2 (indicative of ∼5% of **2b**) and 0.3 (indicative of ∼30% of **2b**). All of these results are consistent with **2a** still being the predominant molecular species of form **2** (in other words, the tautomerization is confirmed to be endergonic), but the fraction of the minor species **2b** can be rather significant.

(3) The ΔpK values describing the relative lability of the axial ligand in forms **1** and **2** are affected by the uncertainty of the pK_t term. The empirically corrected values ($\Delta pK^{int\text{-}PE}$) suggest that the effective lability of the axial ligand in form **2** may be slightly smaller than that in form **1** ($\Delta pK \approx 1$), comparable to it ($\Delta pK \approx 0$) or even 10-fold larger ($\Delta pK \approx -1$). The latter result may seem paradoxical because form **2** is still dominated (≥70%) by the inert hydroxo complex **2a**. However, the unusual effective lability of the axial ligand in this phase is caused by the minor species **2b**, in which the axial

https://doi.org/10.1021/acs.inorgchem.1c00933
Inorg. Chem. 2021, 60, 15948−15967

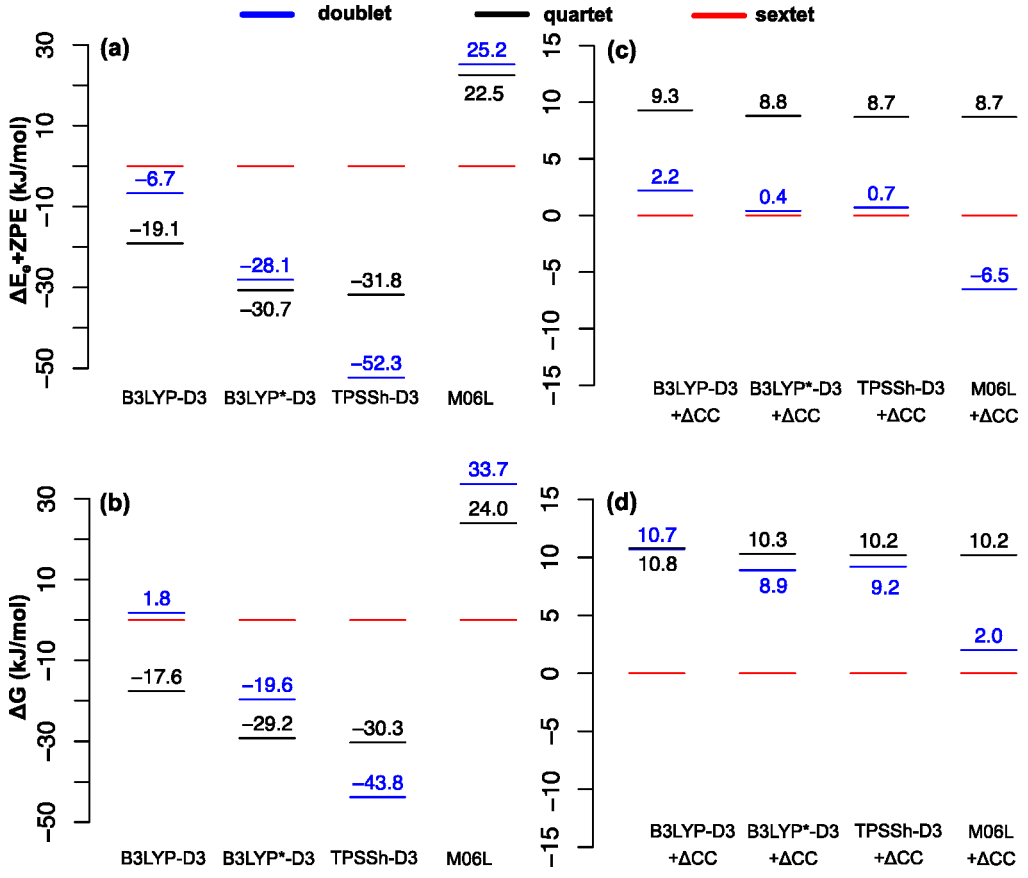

Figure 8. Relative spin-state energetics of complex **1**, i.e., [$Fe^{III}(H_2O)$(HisH)]: (a) zero-point corrected electronic energies (ΔE_e+ZPE) and (b) Gibbs free energies (ΔG for T = 298 K) calculated with four DFT methods: B3LYP-D3, B3LYP*-D3, TPSSh-D3, and M06L, with the PCM solvation model; (c,d) the same quantities at the DFT+ΔCC level. Underlying electronic energies are final estimates obtained from eq 1 or 2.

ligand (having the protonated form) is even more labile than in the labile aqua complex **1**.

Rates of NO Binding. In order to fully interpret the relative k_{on} values determined from the kinetic studies, one also needs to take into account the kinetic factor in eq 13, namely, the relative rates (k_B/k_A) of NO recombination with coordinatively unsaturated complexes **A** and **B**, produced in both forms of AcMP-11 by dissociation of the axial ligand. Based on the fact that both **A** and **B** are predominantly high-spin under the experimental conditions (see next section), whereas the nitrosyl species are low-spin, the formation of the Fe−NO bond is (in both cases) a spin-forbidden reaction, and hence the rate constants k_A and k_B may be below the diffusion limit, as is the case for CO binding to five-coordinate Fe^{II} in deoxy-heme[96] or NO binding to [Fe^{III}(OH)(TMPS)].[18] The electronic structural reorganization that accompanies the Fe−NO bond formation is even more significant than that in the case of Fe−CO bond formation, because the nitrosyl groups in the products have (at least formal) Fe^{II}−NO^+ character, whereas the dissociated fragments are Fe^{III} and $NO^{\cdot}$ and bond formation proceeds through a metastable weakly bound adduct with Fe^{III}−$NO^{\cdot}$ character.[10,97] In this work, we did not attempt to quantitatively describe the k_B/k_A factor—not only due to the challenge in reliable modeling of the reaction rates for such spin-forbidden processes (see, for instance, the recent computational study by Harvey and co-workers[96]) but also in view of the considerable uncertainty caused already by the second factor in eq 13 (relative lability of the axial ligands, $10^{-\Delta pK}$), thus rendering detailed computation of the k_B/k_A factor of limited practical value.

Given that complexes **A** and **B** are similar to each other—they have identical Fe oxidation and spin states (see below) and coordination geometry—the k_A and k_B values may be expected to be comparable. However, deprotonation of the histidine ligand in **B** may influence the rate of ligand binding. In kinetic studies of CO binding to five-coordinate Fe^{II} porphyrins with ImH and Im^- axial ligands,[98,99] Hoffman and co-workers demonstrated that deprotonation of imidazole slows down the CO binding by roughly 2 orders of magnitude. This effect is presumably caused by a stronger Fe−$N_{(imidazole)}$ bond in the five-coordinate complex with deprotonated imidazole, resulting in a larger displacement of the Fe atom out of the porphyrin plane in this complex, and thus a higher energy barrier associated with bond formation (because the Fe needs to be restored toward the porphyrin plane in the six-coordinate product). Assuming that similar factors determine the relative rates of NO recombination with complexes **A** and **B**, it can be assumed that the k_B value is smaller than k_A, perhaps by 1 or 2 orders of magnitude, i.e., $k_B/k_A \sim 10^{-2}$ to 10^{-1}. Such a crude estimate, taken together with the above estimate of the relative lability factor, $10^{-\Delta pK}$, as roughly 10^0 to 10^1 (based on the int-PE empirically corrected estimate of the tautomerization constant), seems to fall in a qualitatively good agreement with the experimental observation that form **2** binds NO by about 1 order of magnitude slower than form **1**.

Spin State Energetics of AcMP-11. Ferric heme complexes of relevance to the proposed reaction mechanism

https://doi.org/10.1021/acs.inorgchem.1c00933
Inorg. Chem. 2021, 60, 15948−15967

(**1**, **2a**, **2b**, **3**, **A**, **B**) may adopt either low-spin (LS; doublet, S = 1/2), intermediate-spin (IS; quartet, S = 3/2), or high-spin (HS; sextet, S = 5/2) states, the relative energies of which are challenging to reliably calculate by DFT methods,[68,100−103] causing problems both with the correct determination of the ground state and with the energy balance for reactions where the ground state changes at the DFT level. A crucial ingredient of our computational studies was to solve this issue by means of the DFT+ΔCC approach, where the error of a given DFT method on the spin-state energetics is approximately corrected for by comparison with reliable coupled cluster results for a simplified model (see Computational Methods and Models). This approach may be viewed as a practical approximation to CCSD(T) calculations for a realistic heme model (too expensive) in which the DFT method is used to describe the difference between the simplified and realistic model, the latter one including not only full ligands but also important hydrogen bonds in the second coordination sphere,[58,59] and the effect of substituents[56] and peptide backbone. The CCSD(T) method, here used in its explicitly correlated formulation to efficiently reach the basis set limit, not only has a reputation of the "gold standard" of computational thermochemistry, including transition metals,[68,69,104−106] but also its accuracy for spin-state energetics has been quantitatively confirmed by comparison with the experimental data.[107,108]

Figure 8 shows bare DFT results and the corresponding DFT+ΔCC results for the spin-state energetics of complex **1**. The energy levels correspond to either zero-point corrected electronic energies (ΔE_e + ZPE; for panels a and c) or the corresponding Gibbs free energies (ΔG at T = 298 K; for panels b and d), both of them relative to the HS state. As is well-known,[103] the difference between the ΔE_e + ZPE and ΔG is mainly caused by the vibrational entropy contribution favoring a higher-spin state with increasing temperature.

A first glance at the bare DFT results in Figure 8a,b already confirms the problem with the strong dependence of the DFT results on the choice of exchange-correlation functional. Four typical DFT methods used here (B3LYP-D3, B3LYP*-D3, TPSSh-D3, M06L) disagree by as much as 70 kJ/mol on the LS−HS relative (free) energy. Moreover, with the exception of M06L, all tested DFT methods predict the IS state to be 20−30 kJ/mol *below* the HS state; in fact, the B3LYP-D3 and B3LYP*-D3 even point to the IS ground state. Such results are contradictory with the experimental reports for **1** having the HS ground state[47] or predominantly HS state in thermal equilibrium with the LS ground state.[35,36,109] Similar issues with overstabilization of the IS state by many DFT methods (here except M06L) were also observed for other heme-related models.[68]

All of these issues are alleviated at the DFT+ΔCC level (Figure 8c,d): not only do the results become practically insensitive to the choice of exchange-correlation functional but also the predicted closeness of the LS and HS states for **1** is in accord with the interpretations of the EPR and UV−vis spectroscopic data.[35,36] Moreover, in contrast to bare DFT results (even M06L, the only one which captures the ordering of HS and IS states qualitatively correct), the DFT+ΔCC results show that the IS state of **1** is *only slightly above* the HS state (within 10 kJ/mol). The HS−IS gap being so small is consistent with an admixture of the IS state with the predominant HS state (due to the spin−orbit coupling, not included in our calculations), a feature inferred from the experimental EPR spectra.[36]

Spin-state energetics for the remaining complexes (**2a**, **2b**, **3**, **A**, and **B**) are analogously reported in Figures S12−S16, Supporting Information. Based on the ΔG values calculated at the B3LYP-D3+ΔCC level, Figure 9 shows the percentage

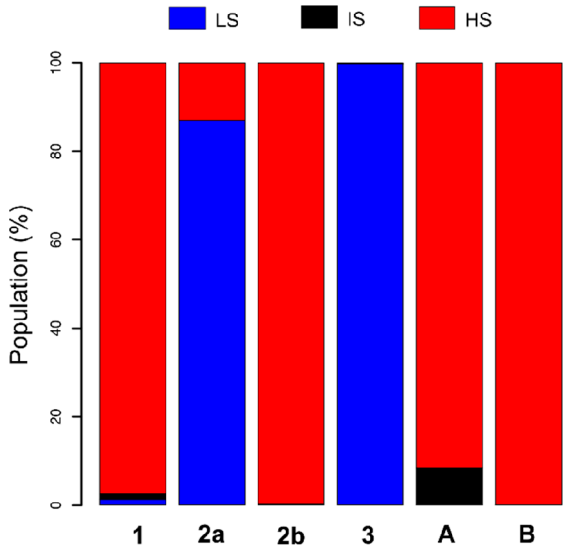

Figure 9. Percentage populations of spin states at 298 K predicted for relevant species of microperoxidase based on the calculated free energies (B3LYP-D3+ΔCC, PCM).

populations of the LS, IS, and HS states for all considered ferric complexes calculated using eq 5. Comparison with B3LYP*-D3+ΔCC, TPSSh-D3+ΔCC, and M06L+ΔCC results can be found in Figures S17−S22, Supporting Information. The majority of our complexes are predicted to be predominantly HS at room temperature, with the notable exception of alkaline species **3** (LS) and **2a** (significant populations of both LS and HS states). The increased stabilization of the LS state for these alkaline species, as compared to **1**, is qualitatively in agreement with the interpretations of the experimental data.[36] Species **A** and **B** of microperoxidase are not experimentally characterized, but five-coordinate monoimidazole complexes analogous to **A**, either synthetic or from cytochromes c′, exhibit extremely labile spin states,[27] suggesting that their HS and IS states are lying close in energy, so that the actual ground state observed in the experiment can be determined by small perturbations of the molecular environment. The closeness of the HS and IS states for species **A** is qualitatively well reproduced by our DFT+ΔCC results (Figure S15, Supporting Information), showing that both states are indeed tightly spaced in energy (within 3 kJ/mol).

Clearly, the accuracy of computed spin-state energetics (even with the CCSD(T) method, here approximated as DFT+ΔCC) is still not high enough[107,108] to permit *quantitative* comparison with the experimental data regarding the LS−HS thermal equilibrium or the spin−orbit admixture of the IS to the HS state. However, the present DFT+ΔCC results appear to be a far more reasonable starting point than bare DFT results to at least *qualitatively* understand the occurrence of these two phenomena.

As a side remark, we would like to note that the experimental data of spin-state energetics for microperoxidases are not far from controversies and therefore may be worth further reinvestigations. For instance, conflicting EPR spectra

https://doi.org/10.1021/acs.inorgchem.1c00933
Inorg. Chem. 2021, 60, 15948−15967

of species **1** of AcMP-11 were reported by different groups,[35,47] and these discrepancies are not accounted for properly. Moreover, all of the currently available EPR spectra were obtained for concentrations which are too high to assume that microperoxidase is monomeric. For instance, the spectra of AcMP-11 were recorded at concentrations ranging from 5.45×10^{-4} M[47] to 2.1×10^{-2} M,[35] although AcMP-11 shows signs of aggregation, possibly due to the formation of μ-oxo bridged structures, already at the concentration of 6.0×10^{-5} M (pH 7.0, room temperature).[47] Under alkaline conditions the aggregation is even more facile, possibly due to formation of other types of dimers (see next section). Low temperature conditions in EPR spectroscopy, in addition, favor this undesired aggregation. The aggregation may also be responsible for the very complicated thermal dependence of the magnetization.[109] The UV−vis and Raman spectra can be recorded at very low concentrations—thus avoiding the aggregation problem—but these spectroscopies provide only indirect information on the microperoxidase spin-state energetics, which is based on literature information on how the Fe(III) spin state in similar systems affects the Soret and Q bands and selected vibrations (see refs 34 and 35 and refs therein).

Behavior of AcMP-11 in Alkaline Solution. Although the behavior of AcMP-11 in a wide range of pH was previously studied[35,36] (see the Introduction), we decided—in view of the unexpected pH-dependent reactivity and registration of doubly exponential kinetic traces for NO binding at alkaline pH—to repeat some of the spectrophotometric titrations and to look closer at the solution behavior of AcMP-11. The studies were performed for 1.5×10^{-5} M and 2.8×10^{-6} M concentrations of AcMP-11. At a first glance, the absorbance changes at a single wavelength of 396 nm coincide with the outcome reported by Marques and result in the determination of two pK_a values, 9.55 and 12.73, similar to the published ones (Figure S8a).[35] However, a more detailed analysis of the overall spectral changes, in particular, the finding that attempts at determining the pK_a values for different wavelengths resulted in widely differing results (Figure S8b), prompted us to apply global fit analysis (Figure S23). The detailed description of the applied approach can be found in the Supporting Information together with the determined pK_a values (Table S10). The general conclusion, drawn from our efforts to analyze the pH-dependent spectral changes using the global fit approach, is that under alkaline pH, where the combination of form **1** and **2** coexists, aggregates are formed at relatively low AcMP-11 concentrations, which is not the case at neutral pH, where only form **1** is present. Additional studies provided further evidence supporting this hypothesis. One of these was a very simple AcMP-11 dilution experiment. Various concentrations of AcMP-11 solutions at pH 11.0 were diluted with a buffer using the stopped-flow technique, and the absorbance change at 396 nm was followed after mixing. AcMP-11 dilution initiated a time dependent absorbance increase in approximately one second. Registered kinetic traces revealed a concentration dependent absorbance change occurring just after dilution, assigned to aggregate decomposition (Figure S24). No such behavior was observed in analogous studies performed at pH 7.4, as well as after mixing equally concentrated solutions at alkaline pH. The commonly used test for aggregate formation is to check whether deviation from Beer's Law occurs. So far the aggregation propensity of AcMP-11 via assessing deviation from Beer's Law has been tested only at pH 6.5, and under such pH conditions no deviation from Beer's Law was observed at least up to 2×10^{-5} M.[35] Analogous studies performed at pH 9.6 revealed that, under alkaline conditions, AcMP-11 aggregates form at concentrations lower than 2×10^{-5} M (Figure S25). Another confirmation for aggregate formation at alkaline pH comes from kinetic studies of NO binding. As mentioned before, a double-exponential function was necessary to properly analyze the registered kinetic traces in the pH range 8.5−11.5. UV−vis spectral changes for slow step did not indicate the formation of a different nitrosylated product than the one obtained in the main/fast reaction step corresponding to monomer reactivity. The percentage fraction of the absorbance change (ΔAbs) for the slow reaction step, with respect to the total absorbance change calculated for both nitrosylation processes (fast and slow) increases with increasing [AcMP-11], which is in agreement with the proposed aggregate formation (Figure S26). Interestingly, pH dependent analysis of the percentage fraction of the ΔAbs for the slow reaction exhibits a pH dependence. Namely, starting from pH 8.5 where kinetic traces have a poorly developed double-exponential character, ΔAbs increases when the pH approaches 10 and then decreases, which corresponds to the fact that, at pH 11.5, the double exponential character of the kinetic traces is barely observable (Figure S27). The described observations point to a certain pH range where the formation of aggregates is favorable, which correlates with the coexistence of forms **1** and **2**. Taking this into account, we postulate that aggregate formation can be associated with the *trans* effect of OH^- in **2a**, the main molecular species of form **2**, resulting in weakening of the Fe−HisH bond (cf. DFT geometries and bond energies in Figure S11, Supporting Information). As a consequence, HisH has the potential to dissociate from the iron center. The "dangling" HisH can replace the labile H_2O ligand in form **1** resulting in the formation of a dimer, having two HisH residues coordinated to one heme (see mechanism proposed in Figure S28, Supporting Information). Such a dimerization mechanism can explain the observation that the preferable pH for aggregate accumulation is around 10, very close to pK_{a1}. At higher pH (>11), where form **2** starts to dominate and form **1** becomes a minor species, the tendency for aggregation is reduced, since one of the crucial reaction partners runs out. Furthermore, accumulation of form **3** with a much stronger Fe−His^- bond (Figure S11) prevents exchanging the "dangling" HisH between two molecules. Our observation concerning the formation of the dimers under alkaline pH are in line with the results reported by van Wart et al., who proposed that, in the same pH range, AcMP-8 forms dimers via His exchange between two microperoxidase molecules.[84] In such a dimer, one AcMP-8 heme center is five-coordinate with hydroxo ligand, whereas the second one is six-coordinate with two-His as axial ligands (Figure S28).[84] We postulate a similar structure for the aggregates that could be the source of complications observed during pH-dependent studies on the reactivity of NO with AcMP-11. However, it cannot be excluded that, under higher AcMP-11 concentrations, μ-oxo-bridged structures can also be formed.

The awareness of dimer formation even at relatively low micromolar concentrations of AcMP-11 is important for realizing that precise determination of pK_a values for ionization of coordinated H_2O could be affected. As confirmed during kinetic studies with NO, traces of aggregates can be observed

https://doi.org/10.1021/acs.inorgchem.1c00933
Inorg. Chem. 2021, 60, 15948−15967

even at AcMP-11 concentrations as low as 2.5×10^{-6} M in the pH range 8.5−11.5.

CONCLUSIONS

The reported pH dependence of the second-order rate constant for NO binding to ferric microperoxidase-11 (AcMP-11) drew our attention to the untypical kinetic profile for the reactivity of its three acid−base related forms (**1**, **2**, and **3**). Individual rate constants for nitrosylation of each form have been determined, showing that doubly deprotonated form **3**, [(AcMP-11)Fe^{III}(OH)(His^-)], is practically inert, whereas singly deprotonated form **2** binds NO by only 1 order of magnitude slower than labile form **1**, [(AcMP-11)Fe^{III}(H_2O)-(HisH)]. Form **2** was so far described as pure [(AcMP-11)Fe^{III}(OH)(HisH)] species, but the inertness of the Fe−OH bond expected for such a six-coordinate porphyrin center (based on the literature and calculated bond energies) does not correspond with the relatively high reaction rate herein determined for **2**. Moreover, the decrease in rate constant on going from **2** to **3**, although the latter one has a weaker Fe−OH bond due to the *trans* His^- effect, shows that the rates of ligand exchange in these alkaline forms of AcMP-11 cannot be accounted for by their Fe−OH bond strengths.

To explain the peculiar reactivity profile, we proposed that for the singly deprotonated form **2**, the dominant molecular species [(AcMP-11)Fe^{III}(OH)(HisH)] (**2a**) coexists with the minor species [(AcMP-11)Fe^{III}(H_2O)(His^-)] (**2b**), being its tautomeric form. The feasibility of the tautomer formation was confirmed by quantum-chemical calculations, although precise determination of the tautomerization constant was not possible due to the challenge in reliably computing relative acidities of the H_2O and HisH ligands. The computational estimates based on the proton exchange scheme suggested that the tautomeric form may be relatively abundant (from a few % up to as much as 30%) in the macroscopic pH-dependent phase **2**. According to that, the reactivity observed under alkaline conditions, where form **2** dominates, is assigned to the NO binding to the tautomeric [(AcMP-11)Fe^{III}(H_2O)(His^-)] species, whose H_2O ligand is even more labile than that in form **1** due to the activating *trans* effect of His^-. The proposed mechanism not only accounts for the unexpectedly high reactivity of form **2** but also explains the inertness of form **3** by the lack of any proton source in it, preventing its tautomerization to labile Fe−OH_2 species.

The present study for the first time points out that the reactivity of a six-coordinate heme center possessing two protic ligands may be influenced by the tautomerization equilibrium in such a way that, although one of these ligands deprotonates preferentially, the minor tautomer with the alternative ligand deprotonation can govern the reactivity. To describe such a situation, the concept of "effective lability" of the axial ligand was coined, taking into account both the excess free energy of the tautomer (inversely related to its equilibrium concentration) and the propensity of the tautomer to dissociatively exchange the ligand. Our results hence suggest that the "effective lability" of the oxygen-based axial ligand in form **2** of AcMP-11 is very high, comparable to the lability of the H_2O ligand in form **1**, although the axial ligand has OH^- character in the majority of molecules belonging to form **2**.

The present study reports a rare example of a well-characterized system where the tautomerism is shown to play a crucial role in the reactivity. Therefore, the reported mechanistic explanations, although established in the specific case study of MP-11, may be of relevance for understanding pH-dependent reaction mechanisms for six-coordinate porphyrins and other transition metal complexes having more than one type of protic ligands. Reported studies may be of interest also for the broader scientific community due to possible catalytic, electrocatalytic, and biomedical applications of this heme peptide.

ASSOCIATED CONTENT

Supporting Information

The Supporting Information is available free of charge at https://pubs.acs.org/doi/10.1021/acs.inorgchem.1c00933.

Additional figures and tables describing experimental and computational details; derivation of eq 19; details of the global fit analysis; total energies and coordinates; complete ref 62, and additional references for the basis sets (PDF)

Atomic coordinates for model types #1 and #2 (TXT)

AUTHOR INFORMATION

Corresponding Authors

Maria Oszajca − *Faculty of Chemistry, Jagiellonian University, 30-387 Krakow, Poland;* orcid.org/0000-0003-2690-0085; Email: maria.oszajca@chemia.uj.edu.pl

Mariusz Radoń − *Faculty of Chemistry, Jagiellonian University, 30-387 Krakow, Poland;* orcid.org/0000-0002-1901-8521; Email: mradon@chemia.uj.edu.pl

Grażyna Stochel − *Faculty of Chemistry, Jagiellonian University, 30-387 Krakow, Poland;* orcid.org/0000-0002-9502-6371; Email: stochel@chemia.uj.edu.pl

Authors

Gabriela Drabik − *Faculty of Chemistry, Jagiellonian University, 30-387 Krakow, Poland*

Alicja Franke − *Department of Chemistry, Ludwigs-Maximilians University, 81377 Munich, Germany;* orcid.org/0000-0002-6318-7429

Rudi van Eldik − *Faculty of Chemistry, Jagiellonian University, 30-387 Krakow, Poland; Department of Chemistry and Pharmacy, University of Erlangen-Nuremberg, 91058 Erlangen, Germany; Faculty of Chemistry, Nicolaus Copernicus University in Torun, 87-100 Torun, Poland;* orcid.org/0000-0003-4271-0118

Complete contact information is available at: https://pubs.acs.org/10.1021/acs.inorgchem.1c00933

Notes

The authors declare no competing financial interest.

ACKNOWLEDGMENTS

The experimental part of this study was supported by National Science Centre, Poland, under the grant number 2016/23/D/ST4/00303. The computational part of this study was supported by National Science Centre, Poland, under the grant number 2017/26/D/ST4/00774, by Jagiellonian University (K/DSC/003792), and by PLGrid Infrastructure (ACK Cyfronet AGH/UST in Krakow and PCSS in Poznan). We thank M.Sc. Janusz Oszajca and Dr. Grzegorz Stopa for support in laser-flash photolysis experiments as well as Dr. Eng. Klaudyna Śpiewak-Wojtyła for support in MP-11 acetylation experiments.

REFERENCES

(1) Traylor, T. G.; Sharma, V. S. Why NO? *Biochemistry* **1992**, *31*, 2847−2849.
(2) Fionda, C.; Pia Abruzzese, M.; Santoni, A.; Cippitelli, M. Immunoregulatory and Effector Activities of Nitric Oxide and Reactive Nitrogen Species in Cancer. *Curr. Med. Chem.* **2016**, *23*, 2618−2636.
(3) Basudhar, D.; Ridnour, L. A.; Cheng, R.; Kesarwala, A. H.; Heinecke, J.; Wink, D. A. Biological signaling by small inorganic molecules. *Coord. Chem. Rev.* **2016**, *306*, 708−723.
(4) Lehnert, N.; Scheidt, W. R. Preface for the inorganic chemistry forum: the coordination chemistry of nitric oxide and its significance for metabolism, signaling, and toxicity in biology. *Inorg. Chem.* **2010**, *49*, 6223−6225.
(5) Franke, A.; Oszajca, M.; Brindell, M.; Stochel, G.; van Eldik, R. Metal-assisted activation of nitric oxide-mechanistic aspects of complex nitrosylation processes. *Adv. Inorg. Chem.* **2015**, *67*, 171−241.
(6) Ford, P. C.; Pereira, J. C. M.; Miranda, K. M. In *Nitrosyl Complexes in Inorganic Chemistry, Biochemistry and Medicine II*; Mingos, D. P. M., Ed.; Springer-Verlag: Berlin, 2014; Vol. *154*, pp 99−136.
(7) Ford, P. C. Reactions of NO and nitrite with heme models and proteins. *Inorg. Chem.* **2010**, *49*, 6226−6239.
(8) Ford, P. C.; Laverman, L. E. Reaction mechanisms relevant to theformation of iron and ruthenium nitric oxide complexes. *Coord. Chem. Rev.* **2005**, *249*, 391−403.
(9) Laverman, L. E.; Hoshino, M.; Ford, P. C. A dissociative mechanism for reactions of nitric oxide with water soluble iron(III) porphyrins. *J. Am. Chem. Soc.* **1997**, *119*, 12663−12664.
(10) Goodrich, L. E.; Paulat, F.; Praneeth, V. K. K.; Lehnert, N. Electronic structure of heme-nitrosyls and its significance for nitric oxide reactivity, sensing, transport, and toxicity in biological systems. *Inorg. Chem.* **2010**, *49*, 6293−6316.
(11) Radoń, M.; Broclawik, E. In *Computational Methods to Study the Structure and Dynamics of Biomolecules and Biomolecular Processes—from Bioinformatics to Molecular Quantum Mechanics*; Liwo, A., Ed.; Springer: Berlin, 2014; pp 711−782.
(12) Laverman, L. E.; Wanat, A.; Oszajca, J.; Stochel, G.; Ford, P. C.; van Eldik, R. Mechanistic studies on the reversible binding of nitric oxide to metmyoglobin. *J. Am. Chem. Soc.* **2001**, *123*, 285−293.
(13) Franke, A.; Stochel, G.; Jung, C.; van Eldik, R. Substrate binding favors enhanced NO binding to $P450_{(cam)}$. *J. Am. Chem. Soc.* **2004**, *126*, 4181−4191.
(14) Jee, J.-E.; Eigler, S.; Hampel, F.; Jux, N.; Wolak, M.; Zahl, A.; Stochel, G.; van Eldik, R. Kinetic and mechanistic studies on the reaction of nitric oxide with a water-soluble octa-anionic iron(III) porphyrin complex. *Inorg. Chem.* **2005**, *44*, 7717−7731.
(15) Franke, A.; Stochel, G.; Suzuki, N.; Higuchi, T.; Okuzono, K.; van Eldik, R. Mechanistic studies on the binding of nitric oxide to a synthetic heme-thiolate complex relevant to cytochrome P450. *J. Am. Chem. Soc.* **2005**, *127*, 5360−5375.
(16) Franke, A.; Hessenauer-Ilicheva, N.; Meyer, D.; Stochel, G.; Woggon, W.-D.; van Eldik, R. Thermodynamic and kinetic studies on the binding of nitric oxide to a new enzyme mimic of cytochrome P450. *J. Am. Chem. Soc.* **2006**, *128* (41), 13611−13624.
(17) Oszajca, M.; Franke, A.; Brindell, M.; Stochel, G.; van Eldik, R. Mechanistic studies on the reactions of cyanide with a water-soluble Fe(III) porphyrin and their effect on the binding of NO. *Inorg. Chem.* **2011**, *50* (8), 3413−3424.
(18) Wolak, M.; van Eldik, R. pH controls the rate and mechanism of nitrosylation of water-soluble Fe^{III} porphyrin complexes. *J. Am. Chem. Soc.* **2005**, *127*, 13312−13315.
(19) Wanat, A.; Wolak, M.; Orzel, L.; Brindell, M.; van Eldik, R.; Stochel, G. Laser flash photolysis as tool in the elucidating of nitric oxide binding mechanism to metallobiomolecules. *Coord. Chem. Rev.* **2002**, *229*, 37−49.
(20) Ford, P. C.; Laverman, L. E.; Lorkovic, I. M. Reaction mechanisms of nitric oxide with biologically relevant metal centers. *Adv. Inorg. Chem.* **2003**, *54*, 203−257 and references therein.
(21) Ford, P. C.; Lorkovic, I. M. Mechanistic aspects of the reactions of Nitric Oxide with transition-metal complexes. *Chem. Rev.* **2002**, *102*, 993−1018 and references therein.
(22) Laverman, L. E.; Ford, P. C. Mechanistic studies of nitric oxide reactions with water soluble Iron(II), Cobalt(II), and Iron(III) porphyrin omplexes in aqueous solutions:implications for biological activity. *J. Am. Chem. Soc.* **2001**, *123*, 11614−11622.
(23) Hoshino, M.; Ozawa, K.; Seki, H.; Ford, P. C. Photochemistry of nitric oxide adducts of water-soluble iron(III) porphyrin and ferrihemoproteins studied by nanosecond laser photolysis. *J. Am. Chem. Soc.* **1993**, *115*, 9568.
(24) Franke, A.; van Eldik, R. Factors that determine the mechanism of NO activation by metal complexes of biological and environmental relevance. *Eur. J. Inorg. Chem.* **2013**, *2013*, 460−480 and references therein.
(25) Zhao, Y.; Hoganson, C.; Babcock, G. T.; Marletta, M. A. Structural Changes in the Heme Proximal Pocket Induced by Nitric Oxide Binding to Soluble Guanylate Cyclase. *Biochemistry* **1998**, *37*, 12458−12464.
(26) Ikezaki, A.; Nakamura, M. Models for cytochromes c': spin states of mono(imidazole)-ligated (meso-tetramesitylporphyrinato)-iron(III) complexes as studied by UV-Vis, 13 C NMR, 1 H NMR, and EPR spectroscopy. *Inorg. Chem.* **2002**, *41*, 6225−6236.
(27) Ikezaki, A.; Takahashi, M.; Nakamura, M. Models for cytochromes c′: observation of an extremely labile spin state in monoimidazole complexes of saddle-shaped iron(III) porphyrinates. *Angew. Chem.* **2009**, *121*, 6418−6421.
(28) Kalaivani, G.; Sivanesan, A.; Kannan, A.; Sevvel, R. Generating monomeric 5-coordinated microperoxidase-11 usingcarboxylic acid functionalized silver nanoparticles: Asurface-enhanced resonance Raman scattering analysis. *Colloids Surf., B* **2016**, *146*, 722−730.
(29) Heleg-Shabtai, V.; Katz, E.; Willner, I. Assembly of Micro-peroxidase-11 and Co(II)-Protoporphyrin IX Reconstituted Myoglo-bin Monolayers on Au-Electrodes:Integrated Bioelectrocatalytic Interfaces. *J. Am. Chem. Soc.* **1997**, *119*, 8121−8122.
(30) Zhu, X.; Yuri, I.; Gan, X.; Suzuki, I.; Li, G. Electrochemical study of the effect ofnano-zinc oxide on microperoxidase and its application to more sensitivehydrogen peroxide biosensor prepara-tion. *Biosens. Bioelectron.* **2007**, *22*, 1600−1604.
(31) Willmer, I. Crosslinked integrated enzyme electrodes for bioelectronicapplications. *Acta Polym.* **1998**, *49*, 652−662.
(32) Renault, C.; Andrieux, C. P.; Tucker, R. T.; Brett, M. J.; Balland, V.; Limoges, B. Unraveling the Mechanism of Catalytic Reduction of O_2 by Microperoxidase-11 Adsorbed within a Transparent 3D-Nanoporous ITO Film. *J. Am. Chem. Soc.* **2012**, *134*, 6834−6845.
(33) Lykourinou, V.; Chen, Y.; Wang, X.-S.; Meng, L.; Hoang, T.; Ming, L.-J.; Musselman, R. L.; Ma, S. Immobilization of MP-11 into a Mesoporous Metal Organic Framework, MP-11@mesoMOF: A New Platform for Enzymatic Catalysis. *J. Am. Chem. Soc.* **2011**, *133*, 10382−10385.
(34) Munro, O. Q.; Marques, H. M. Heme-peptide models for hemoproteins. 1. Solution chemistry of N-acetylmicroperoxidase-8. *Inorg. Chem.* **1996**, *35*, 3752−3767.
(35) Marques, H. M.; Perry, C. B. Hemepeptide models for hemoproteins: the behavior of N-acetylmicroperoxidase-11 in aqueous solution. *J. Inorg. Biochem.* **1999**, *75* (75), 281−291.
(36) Marques, H. M. Insights into porphyrin chemistry provided by the microperoxidases, the haempeptides derived from cytochrome c. *Dalton. Trans.* **2007**, 4371−4385.
(37) Nazari, K.; Mahmoudi, A.; Khosraneh, M.; Haghighian, Z.; Moosavi-Movahedi, A. A. Kinetic analysis for suicide-substrate inactivation of microperoxidase-11: A modified model for bisubstrate enzymes in the presence of reversible inhibitors. *J. Mol. Catal. B: Enzym.* **2009**, *56*, 61−69.

https://doi.org/10.1021/acs.inorgchem.1c00933
Inorg. Chem. 2021, 60, 15948−15967

(38) Jeng, W.-Y.; Tsai, Y.-H.; Chuang, W.-J. The catalase activity of N3833. *J. Pept. Res.* **2004**, *64*, 104−109.
(39) O'Reilly, N. J.; Magner, E. The effect of solvent on the catalytic properties of microperoxidase-11. *Phys. Chem. Chem. Phys.* **2011**, *13*, 5304−5313.
(40) Reszka, K. J.; McCormick, M. L.; Britigan, B. E. Oxidation of antracycline anticancer agents by the peroxidase mimic microperoxidase 11 and hydrogen peroxide. *Free Radical Biol. Med.* **2003**, *35*, 78−93.
(41) Ascenzi, P.; Sbardella, D.; Santucci, R.; Coletta, M. Cyanide binding to ferrous and ferric microperoxidase-11. *JBIC, J. Biol. Inorg. Chem.* **2016**, *21*, 511−522.
(42) Boubeta, F. M.; Bieza, S. A.; Bringas, M.; Estrin, D. A.; Boechi, L.; Bari, S. E. Mechanism of sulfide binding by ferric hemeproteins. *Inorg. Chem.* **2018**, *57*, 7591−7600.
(43) Lee, T.; Kim, J.; Park, J.; Pak, Y.; Kim, H.; Lim, M. Rebinding dynamics of NO to microperoxidase-8 probed by time-resolved vibrational spectroscopy. *Phys. Chem. Chem. Phys.* **2016**, *18*, 5192−5202.
(44) Galardon, E.; Huguet, F.; Herrero, C.; Ricoux, R.; Artaud, I.; Padovani, D. Reactions of persulfides with the heme cofactor of oxidized myoglobin and microperoxidase 11: reduction or coordination. *Dalton Trans.* **2017**, *46*, 7939−7946.
(45) Marques, H. M.; Baldwin, D. A.; Pratt, J. M. Hemes and hemoproteins. 3. The reaction of microperoxidase-8 with cyanide: comparison with aquocobalamin and hemoproteins. *J. Inorg. Biochem.* **1987**, *29*, 77−91.
(46) Ascenzi, P.; De Simone, G.; Sbardella, D.; Coletta, M. Reductive nitrosylation of ferric microperoxidase-11. *JBIC, J. Biol. Inorg. Chem.* **2019**, *24*, 21−29.
(47) Carraway, A. D.; McCollum, M. G.; Peterson, J. Characterization of N-acetylated heme undecapeptide and some of Its derivatives in aqueous media: monomeric model systems for hemoproteins. *Inorg. Chem.* **1996**, *35*, 6885−6891.
(48) Mathura, S.; Sannasy, D.; de Sousa, A. S.; Perry, C. B.; Navizet, I.; Marques, H. M. The preparation of N-acetyl-Co(III)-microperoxidase-8 (NAcCoMP8) and its ligand substitution reactions: A comparison with aquacobalamin (vitamin B12a). *J. Inorg. Biochem.* **2013**, *123*, 66−79.
(49) Ryabova, E. S.; Rydberg, P.; Kolberg, M.; Harbitz, E.; Barra, A.-L.; Ryde, U.; Andersson, K. K.; Nordlander, E. A comparative reactivity study of microperoxidases based on hemin, mesohemin and deuterohemin. *J. Inorg. Biochem.* **2005**, *99*, 852−63.
(50) Phung, Q. M.; Feldt, M.; Harvey, J. N.; Pierloot, K. Towards Highly Accurate Spin State Energetics in First-Row Transition Metal Complexes: A Combined CASPT2/CC Approach. *J. Chem. Theory Comput.* **2018**, *14* (5), 2446−2455.
(51) Stoneburner, S. J.; Truhlar, D. G.; Gagliardi, L. Transition Metal Spin-State Energetics by MC-PDFT with High Local Exchange. *J. Phys. Chem. A* **2020**, *124* (6), 1187−1195.
(52) Diamantis, A. A.; Dubrawski, J. V. Preparation and structure of ethylenediaminetetraacetate complexes of ruthenium(II) with dinitrogen, carbon monoxide, and other a-acceptor ligands. *Inorg. Chem.* **1981**, *20*, 1142−1150.
(53) Spitzer, M.; Gärtig, F.; van Eldik, R. Compact, transportable, and multipurpose high-pressure unit for UV-VIS spectroscopic measurements at pressures up to 200 MPa. *Rev. Sci. Instrum.* **1988**, *59*, 2092−2093.
(54) van Eldik, R.; Gaede, W.; Wieland, S.; Kraft, J.; Spitzer, M.; Palmer, D. A. Spectrophotometric stopped-flow apparatus suitable for high-pressure experiments to 200 MPa. *Rev. Sci. Instrum.* **1993**, *64*, 1355−1357.
(55) van Eldik, R.; Palmer, D. A.; Schmidt, R.; Kelm, H. Volumes of activation for the anation of Pd(II) substituted dien complexes by chloride ion in aqueous solution. A high pressure stopped-flow instrument for studying the kinetics of fast reactions under pressure. *Inorg. Chim. Acta* **1981**, *50*, 131−135.
(56) Kepp, K. P. Heme isomers substantially affect heme's electronic structure and function. *Phys. Chem. Chem. Phys.* **2017**, *19*, 22355−22362.
(57) Ogliaro, F.; Cohen, S.; de Visser, S. P.; Shaik, S. Medium Polarization and Hydrogen Bonding Effects on Compound I of Cytochrome P450: What Kind of Radical Is It Really? *J. Am. Chem. Soc.* **2000**, *122*, 12892−12893.
(58) Jensen, K.; Ryde, U. Importance of proximal hydrogen bonds in haem proteins. *Mol. Phys.* **2003**, *101* (13), 2003−2018.
(59) Sahoo, D.; Quesne, M. G.; de Visser, S. P.; Rath, S. P. Hydrogen-Bonding Interactions Trigger a Spin-Flip in Iron(III) Porphyrin Complexes. *Angew. Chem., Int. Ed.* **2015**, *54*, 4796−4800.
(60) Radoń, M.; Drabik, G. Spin States and Other Ligand–Field States of Aqua Complexes Revisited with Multireference Methods Including Solvation Effects. *J. Chem. Theory Comput.* **2018**, *14*, 4010−4027.
(61) Grimme, S.; Ehrlich, S.; Goerigk, L. Effect of the damping function in dispersion corrected density functional theory. *J. Comput. Chem.* **2011**, *32*, 1456−1465.
(62) Frisch, M. J. et al. *Gaussian 09*, revision D.01; Gaussian Inc.: Wallingford CT, 2009 (complete reference in Supporting Information).
(63) Tomasi, J.; Mennucci, B.; Cammi, R. Quantum Mechanical Continuum Solvation Models. *Chem. Rev.* **2005**, *105*, 2999−3094.
(64) Marenich, A. V.; Cramer, C. J.; Truhlar, D. G. Universal solvation model based on solute electron density and on a continuum model of the solvent defined by the bulk dielectric constant and atomic surface tensions. *J. Phys. Chem. B* **2009**, *113*, 6378−6396.
(65) Wertz, D. H. Relationship between the gas-phase entropies of molecules and their entropies of solvation in water and 1-octanol. *J. Am. Chem. Soc.* **1980**, *102*, 5316−5322.
(66) Cooper, J.; Ziegler, T. A density functional study of SN2 substitution at square-planar platinum(II) complexes. *Inorg. Chem.* **2002**, *41*, 6614−6622.
(67) Léonard, C.; Le Quéré, F.; Adjei, D.; Denisov, S. A.; Mostafavi, M.; Archirel, P. Oxidation of silver cyanide $[Ag(CN)_2]^-$ by the OH radical: From Ab initio calculation to molecular simulation and to experiment. *J. Phys. Chem. A* **2020**, *124*, 10787−10798.
(68) Radoń, M. Spin-state energetics of heme-related models from DFT and coupled cluster calculations. *J. Chem. Theory Comput.* **2014**, *10*, 2306−2321.
(69) Radoń, M. Role of spin states in nitric oxide binding to cobalt(II) and manganese(II) porphyrins. Is tighter binding always stronger? *Inorg. Chem.* **2015**, *54*, 5634−5645.
(70) Knizia, G.; Adler, T. B.; Werner, H.-J. Simplified CCSD(T)-F12 methods: Theory and benchmarks. *J. Chem. Phys.* **2009**, *130*, 054104.
(71) Werner, H.-J.; Knowles, P. J.; Knizia, G.; Manby, F. R.; Schütz, M. et al. *MOLPRO*, version 2019.2; Cardiff University: Cardiff, U.K.; Universität Stuttgart: Stuttgart, Germany, **2019**. See http://www.molpro.net.
(72) Ho, J.; Coote, M. L. First-principles prediction of acidities in the gas and solution phase. *Wiley Interdiscip. Rev.: Comput. Mol. Sci.* **2011**, *1*, 649−660.
(73) Ho, J. Are thermodynamic cycles necessary for continuum solvent calculation of pKas and reduction potentials? *Phys. Chem. Chem. Phys.* **2015**, *17*, 2859−2868.
(74) Sharma, V. S.; Isaacson, R. A.; John, M. E.; Waterman, M. R.; Chevion, M. Reaction of nitric oxide with heme proteins: studies on metmyoglobin, opossum methemoglobin, and microperoxidase. *Biochemistry* **1983**, *22*, 3897−3902.
(75) Wanat, A.; Schneppensieper, T.; Karocki, A.; Stochel, G.; van Eldik, R. Thermodynamics and kinetics of Ru-III(edta) as an efficient scavenger for nitric oxide in aqueous solution. *J. Chem. Soc., Dalton Trans.* **2002**, 941−950.
(76) Jee, J.-E.; Wolak, M.; Balbinot, D.; Jux, N.; Zahl, A.; van Eldik, R. A comparative mechanistic study of the reversible binding of NO to a water-soluble octa-cationic Fe^{III} porphyrin complex. *Inorg. Chem.* **2006**, *45*, 1326−1337.

https://doi.org/10.1021/acs.inorgchem.1c00933
Inorg. Chem. 2021, 60, 15948−15967

(77) Jee, J.-E.; Eigler, S.; Jux, N.; Zahl, A.; van Eldik, R. Influence of an extremely negatively charged porphyrin on the reversible binding kinetics of NO to Fe(III) and the subsequent reductive nitrosylation. *Inorg. Chem.* **2007**, *46*, 3336−3352.
(78) Ashley, K. R.; Leipoldt, J. G.; Joshi, V. K. Kinetic and equilibrium study of the reaction of (meso-tetrakis(p-sulfonatophenyl)porphinato)diaquochromat (III) with thiocyanate ion in aqueous solution. *Inorg. Chem.* **1980**, *19*, 1608−1612.
(79) Pasternack, R. F.; Cobb, M. A. The substitution reactions of a water soluble cobalt(III) porphyrin with thiocyanate as a function of pH. *J. Inorg. Nucl. Chem.* **1973**, *35*, 4327−4339.
(80) Pasternack, R. F.; Parr, G. R. Substitution reactions of tetracarboxyphenylporphinatocobaltate(III) with thiocyanate and pyridine as a function of pH. *Inorg. Chem.* **1976**, *15*, 3087−3093.
(81) Leipoldt, J. G.; Basson, S. S.; Potgieter, I. M.; Roodt, A. Kinetic study of the reaction between trans-dioxotetracyanomolybdate(IV) ions and 1,10-phenanthroline. *Inorg. Chem.* **1987**, *26*, 57−59.
(82) Samotus, A.; Kanas, A.; Glug, W.; Szklarzewicz, J.; Burgess, J. Kinetic study of the reaction between protonatedtrans-dioxotetracyanomolybdate(IV) and 2,2′-bipyridyl. *Transition Met. Chem.* **1991**, *16*, 614−617.
(83) Roodt, A.; Basson, S. S.; Leipoldt, J. G. Studies on the substitution reactions of dioxotetracyanometalate systems with bidentate ligands: kinetics of the reaction between aquaoxotetracyanotungstate(IV) and 2-pyridinecarboxylate ions. *Polyhedron* **1994**, *13*, 599−607.
(84) Wang, J.-S.; Tsai, A.-L.; Heldt, J.; Palmer, G.; van Wart, H. E. Temperature- and pH-dependent changes in the coordination sphere of the heme c group in the model peroxidase N8488. *J. Biol. Chem.* **1992**, *267*, 15310−15318.
(85) Walbe, H.; Isensee, R. W. Notes - Spectrophotometric Study of the Acid Strength of Imidazole. *J. Org. Chem.* **1956**, *21* (6), 702−704.
(86) Thapa, B.; Schlegel, H. B. Improved pKa Prediction of Substituted Alcohols, Phenols, and Hydroperoxides in Aqueous Medium Using Density Functional Theory and a Cluster-Continuum Solvation Model. *J. Phys. Chem. A* **2017**, *121* (24), 4698−4706.
(87) Thapa, B.; Raghavachari, K. Accurate pKa Evaluations for Complex Bio-Organic Molecules in Aqueous Media. *J. Chem. Theory Comput.* **2019**, *15* (11), 6025−6035.
(88) Xu, L.; Coote, M. L. Methods To Improve the Calculations of Solvation Model Density Solvation Free Energies and Associated Aqueous pKa Values: Comparison between Choosing an Optimal Theoretical Level, Solute Cavity Scaling, and Using Explicit Solvent Molecules. *J. Phys. Chem. A* **2019**, *123* (34), 7430−7438.
(89) Heimdal, J.; Kaukonen, M.; Srnec, M.; Rulíšek, L.; Ryde, U. Reduction Potentials and Acidity Constants of Mn Superoxide Dismutase Calculated by QM/MM Free-Energy Methods. *ChemPhysChem* **2011**, *12* (17), 3337−3347.
(90) Gilson, R.; Durrant, M. C. Estimation of the pKa values of water ligands in transition metal complexes using density functional theory with polarized continuum model solvent corrections. *Dalton Trans.* **2009**, 10223−10230.
(91) Galstyan, G.; Knapp, E. W. Computing pKA values of hexa-aqua transition metal complexes. *J. Comput. Chem.* **2015**, *36* (2), 69−78.
(92) Bryantsev, V. S.; Diallo, M. S.; Goddard, W. A. Computational Study of Copper(II) Complexation and Hydrolysis in Aqueous Solutions Using Mixed Cluster/Continuum Models. *J. Phys. Chem. A* **2009**, *113* (34), 9559−9567.
(93) Jerome, S. V.; Hughes, T. F.; Friesner, R. A. Accurate pKa Prediction in First-Row Hexaaqua Transition Metal Complexes Using the B3LYP-DBLOC Method. *J. Phys. Chem. B* **2014**, *118* (28), 8008−8016.
(94) Saito, K.; Nakagawa, M.; Ishikita, H. pKa of the ligand water molecules in the oxygen-evolving Mn4CaO5 cluster in photosystem II. *Communications Chemistry* **2020**, *3* (1), 89.
(95) Grauffel, C.; Chu, B.; Lim, C. An efficient protocol for computing the pKa of Zn-bound water. *Phys. Chem. Chem. Phys.* **2018**, *20*, 29637−29647.
(96) Lábas, A.; Menyhárd, D. K.; Harvey, J. N.; Oláh, J. First Principles Calculation of the Reaction Rates for Ligand Binding to Myoglobin: The Cases of NO and CO. *Chem. - Eur. J.* **2018**, *24*, 5350−5358.
(97) Park, J.; Lee, T.; Lim, M. Direct Observation of the Low-Spin Fe(III)-NO(radical) Intermediate State during Rebinding of NO to Photodeligated Ferric Cytochrome c. *J. Phys. Chem. B* **2013**, *117* (40), 12039−12050.
(98) Stanford, M. A.; Swartz, J. C.; Phillips, T. E.; Hoffman, B. M. Electronic control of ferroporphyrin ligand-binding kinetics. *J. Am. Chem. Soc.* **1980**, *102* (13), 4492−4499.
(99) Swartz, J. C.; Stanford, M. A.; Moy, J. N.; Hoffman, B. M.; Valentine, J. S. Kinetics of carbon monoxide binding to Fe(TPP)(Im) and Fe(TPP)(Im-): evidence regarding protein control of heme reactivity. *J. Am. Chem. Soc.* **1979**, *101* (12), 3396−3398.
(100) Swart, M. In *New Directions in the Modeling of Organometallic Reactions*; Springer: Cham, 2020; Vol. *67*, pp 191−226.
(101) Siig, O.; Kepp, K. P. Iron(II) and Iron(III) Spin Crossover: Toward an Optimal Density Functional. *J. Phys. Chem. A* **2018**, *122* (16), 4208−4217.
(102) Cirera, J.; Via-Nadal, M.; Ruiz, E. Benchmarking Density Functional Methods for Calculation of State Energies of First Row Spin-Crossover Molecules. *Inorg. Chem.* **2018**, *57* (22), 14097−14105.
(103) Kepp, K. P. In *Transition Metals in Coordination Environments: Computational Chemistry and Catalysis Viewpoints*; Broclawik, E., Borowski, T., Radoń, M., Ed.; Springer International Publishing: Cham, 2019; Vol. *29*, pp 1−33.
(104) Olah, J.; Harvey, J. NO bonding to heme groups: DFT and correlated ab initio calculations. *J. Phys. Chem. A* **2009**, *113*, 7338−7345.
(105) Fang, Z.; Vasiliu, M.; Peterson, K. A.; Dixon, D. A. Prediction of bond dissociation energies/heat of formation for diatomic transition metal compounds: CCSD(T) works. *J. Chem. Theory Comput.* **2017**, *13*, 1057−1066.
(106) Flöser, B. M.; Guo, Y.; Riplinger, C.; Tuczek, F.; Neese, F. Detailed pair natural orbital-based coupled cluster studies of spin crossover energetics. *J. Chem. Theory Comput.* **2020**, *16*, 2224−2235.
(107) Drabik, G.; Szklarzewicz, J.; Radoń, M. Spin-state energetics of metallocenes: How do best wave function and density functional theory results compare with the experimental data? *Phys. Chem. Chem. Phys.* **2021**, *23*, 151−172.
(108) Radoń, M. Benchmarking quantum chemistry methods for spin-state energetics of iron complexes against quantitative experimental data. *Phys. Chem. Chem. Phys.* **2019**, *21*, 4854−4870.
(109) Munro, O. Q.; de Wet, M.; Pollak, H.; van Wyk, J.; Marques, H. M. Haempeptide models for haemoproteins, Part 3. N-Acetylmicroperoxidase-8: EPR, Mössbauer and magnetic susceptibility studies on an iron(III) porphyrin in thermal equilibrium between S = 3/2, 5/2 and S = 1/2 states. *J. Chem. Soc., Faraday Trans.* **1998**, *94* (12), 1743−1752.

https://doi.org/10.1021/acs.inorgchem.1c00933
Inorg. Chem. 2021, 60, 15948−15967